Drag reduction by rotary oscillation for flow past a circular cylinder

Yogesh G. Bhumkar, Tapan K. Sengupta,[1]
Department of Aerospace Engineering,
Indian Institute of Technology Kanpur, Kanpur 208016, India

Abstract
With the help of computational results of incompressible flow past a circular cylinder at Reynolds numbers of *Re* = 150 and 1000, we explain two possible mechanisms for the experimentally observed drag reduction by rotary oscillation. Here, detailed computed results are compared with available experimental and computational results in Thiria *et al*. (J Fluid Mech 2006; 560:123–147) for *Re* = 150. The time-varying loads and moments for various cases have been analyzed first to study bluff body flow control at low Reynolds numbers. We specifically focus upon the effects of amplitude and frequency of the rotary oscillation. Furthermore, to study the effects of Reynolds number, we report another case for a higher Reynolds number of *Re* = 1000. Proper orthogonal decomposition of computational data for these two *Re* cases have been performed to explain physical mechanisms behind drag reduction by rotary oscillation and reduced order modeling for different parameter combinations. We show that the drag reduction at the lower Reynolds number (*Re* = 150) is related to organization of the larger shed vortices in the wake with the presence or absence of subharmonics. At the higher Reynolds number (*Re* = 1000), this is achieved by breaking the larger vortices into smaller ones by imposed surface motion that we term as aerodynamic tripping. This is related to the bypass transition-triggered by unsteady separation of the kind discussed in literature.

Keywords: Bluff body flows; Flow control; Drag Reduction; Aerodynamic Tripping; Bypass Transition

1 INTRODUCTION

Bluff-body flow control by rotary oscillation to alter wake geometry and vortex shedding pattern is a problem of significant practical and research interest. Studies of flow over an oscillating circular cylinder have focused earlier on either in-line or transverse rectilinear oscillations, as reviewed by Bearman [1], Berger & Willie [2], Griffin & Hall [3], Sumer & Fredsφe [4] and in Williamson & Govardhan [5]. These studies are considered important, as such oscillations occur for nominally stationary cylinder in uniform flow due to elastic deflections of the cylinder. At the same time, there also exist significant interest to control flow past bluff bodies to reduce drag and unsteadiness by imposed oscillation. Flow past a steadily rotating circular cylinders reported in Badr *et al*. [6], Chang & Chern [7], Chen *et al*. [8], Sengupta *et al*. [9] and other references show drag reduction. At higher rotation rates and moderate Reynolds numbers, vortex shedding was shown to be suppressed in Diaz *et al*. [10] by steadily rotating the circular cylinder. Pure rotation does not work for other bluff bodies and this has motivated researchers to investigate flow control by other means- one such method is shown schematically in Fig. 1 by rotary oscillation of the cylinder. The qualitative difference between steady and oscillatory rotation strategies reveal that in case of former, the controlled flow approaches the inviscid limit (see however the discussion in Sengupta *et al*. [9] on the final equilibrium flow decided by viscous instability). For rotary oscillation, laminar flow over the cylinder is aerodynamically tripped by unsteady separation- as discussed in Sengupta *et al*. [11] and Sengupta & Kumar [12]. Thus, rotary oscillation causes vigorous drag crisis at lower Reynolds numbers as compared to uncontrolled cases where it occurs naturally at higher Reynolds numbers or at relatively lower *Re* caused by surface roughness. Rotary oscillation of a geometrically smooth cylinder causing drag reduction at lower Reynolds numbers is the subject of present study.

[1]Corresponding author; Phone no. +91 512 2597945; e-mail: bhumkar@iitk.ac.in (Yogesh G. Bhumkar)

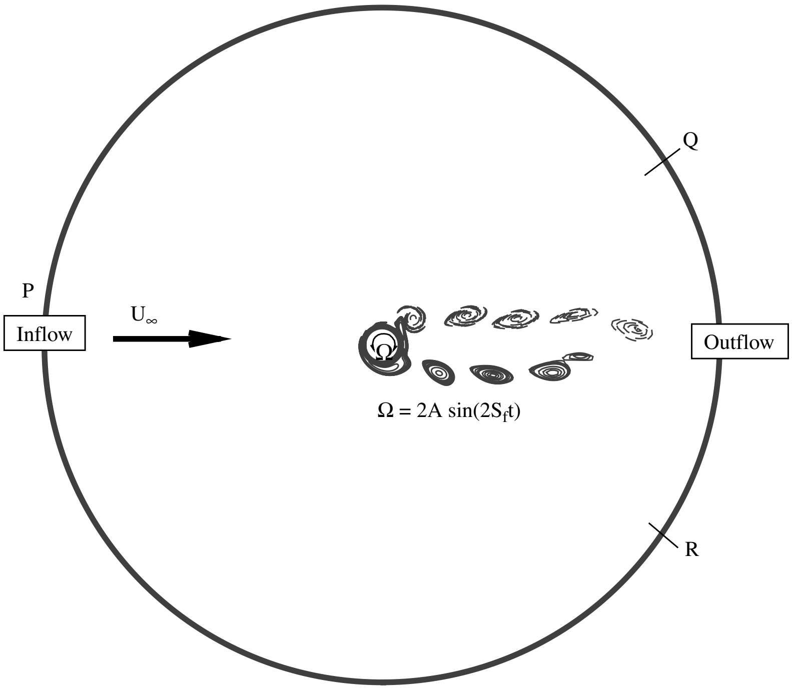

Fig. 1. Schematic of the flow past a circular cylinder executing rotary oscillation (Ω). The outer boundary of the computational domain is composed of the inflow (arc-RPQ) and the outflow (arc-QR).

Flow control by rotary oscillation for circular cylinder is governed by three major parameters. Here we follow the convention of referring dimensional quantities with asterisk and non-dimensional quantities without it. The first non-dimensional parameter is the Reynolds number, defined as $Re = U^*_\infty d^*/\nu^*$, where U^*_∞ is translational speed of the cylinder of diameter d^* and ν^* is the kinematic viscosity of the fluid . If f_f^* is the forcing frequency, then the second important non-dimensional parameter Strouhal number (S_f) and the non-dimensional time scale (t) are obtained by $S_f = f_f^* d^*/U^*_\infty$ and $t = t^* U^*_\infty/d^*$. The maximum non-dimensional angular excursion θ_0 is related to the maximum rotation rate Ω^*_1 as $\Omega^*_1 = 2\pi f^*_f \theta_0$. From the above parameters instantaneous rotation rate Ω^* is given by,

$$\Omega^* = \Omega^*_1 \sin\,(2S_f\, t) \tag{1}$$

Non-dimensional surface speed A is the third important parameter and can be written as $A = \Omega^*_1 d^* /2U^*_\infty$. Here, all the equations have been solved in non-dimensional form with d^* as the length scale and U^*_∞ as the velocity scale and the non-dimensional maximum rotation rate is given by $\Omega_1 = 2A$. Pressure is non-dimensionalized by $\rho^* U^{*2}_\infty$ in the formulation. We non-dimensionalize f_f^* by the natural frequency (f_0^*) of the unforced case at Re = 150 and the corresponding non-dimensional parameter is referred as f_f/f_0 in the present manuscript. We have reported results with f_f/f_0 and used S_f only to relate it with notations used in Dennis *et al*. [13] and some other references.

In Taneda [14], flow visualization results for $30 \le Re \le 300$ have shown the qualitative alteration of vortex shedding behind circular cylinder by rotary oscillation. It was noted that for $Re = 40$ and $11.5\pi < S_f < 27\pi$, vortex shedding was completely eliminated. In Okajima *et al*. [15], forces acting on cylinder for $40 \le Re \le 160$ and $3050 \le Re \le 6100$ were measured for $0.2 \le \Omega_1 \le 1.0$ and $0.025\pi \le S_f \le 0.15\pi$. Similar results were reported in Wu *et al*. [16] for Re = 300 and 500. In Tokumaru & Dimotakis [17], experimental finding of drag reduction by more than 80% was reported for Re = 15,000. Drag was calculated from the wake survey of mean velocity profile, not considering the contribution from fluctuating velocity components. An alteration of Karman vortex shedding by rotary oscillation in the range $250 \le Re \le 1200$ was reported in Filler *et al*.[18], with peripheral speed between 0.5% and 3% of U_∞. Thiria *et al*. [19] have provided a very detailed set of results for this flow field at Re = 150 over a wide range of A and f_f.

There are only some numerical results in the literature for higher Reynolds numbers. Navier-Stokes equation was solved in Lu & Sato [20] for the parameters : Re = 200, 1000, 3000; $0.1 \leq \Omega_1 \leq 3.0$ and $0.5\pi \leq S_f \leq 4\pi$. Baek & Sung [21] reported results for Re = 110 at very low peak rotation rates and Strouhal numbers. Dennis *et al.* [13] used stream function- vorticity formulation to solve Navier-Stokes equation by a spectral-finite difference method for Re = 500 and 1000. Major observations [13] relate to the presence of co-rotating vortex pairs and a time variation of drag coefficient that switches frequency abruptly at a discrete time for Re = 500, $\Omega_1 = 1$ and $S_f = \pi/2$. The authors also reported strong dependence of the flow on Re, as opposed to the earlier observation of Lu & Sato [20]. There are other low to moderate Reynolds number simulations of the Navier-Stokes equation reported in Cheng *et al.* [22] and Choi *et al.* [23]. Flow control and optimization studies were undertaken in Protas & Styczek [24] and He *et al.* [25]. In Sengupta *et al.* [11] a case of rotary oscillation was studied for Re = 15,000 to find out a real-time strategy to control flow past a cylinder using genetic algorithm. The same numerical method is used in the present investigation. The main motivation in the present study is to understand the physical mechanisms those lead to drag reduction for the flow at low to moderate Reynolds numbers. In Sengupta & Kumar [12], this flow was studied for Re = 1000, with the control imposed by simultaneous steady and rotary oscillation of the cylinder. Proper orthogonal decomposition (POD) of the data revealed that a single vortical structure in the base region for the uncontrolled case weakens by rotary oscillation leaving a weaker vortex street. With control, importance of multiple modes reduces as the leading mode accounts for 98% for the case of $\Omega_1 = 1$, as compared to the leading mode of the uncontrolled case ($\Omega_1 = 0$) that accounts for only 40% of the total enstrophy.

Shiels & Leonard [26] studied the two-dimensional flow for Re = 15,000 using a high resolution viscous vortex method to understand the physical mechanism behind drag reduction. The results were produced up to a distance of *5d* from the cylinder, for small computational times without computing the loads on the cylinder. Also, results did not show convergence with number of vortices used to simulate the flow. However, the authors noted *multi-pole vorticity structures* for particular cases of rotary oscillation, revealing bursting phenomenon in the boundary layer. Similar phenomenon of vortical eruption in shear layers have been reported in Sengupta *et al.* [27], Lim *et al.* [28] and have been termed as bypass transition. This bypass transition was attributed for large drag reduction- a phenomenon not present at low Reynolds number simulations. The present investigation also supports this observation that the drag reduction at low and moderate Reynolds numbers occur due to different physical mechanisms. Protas & Wesfreid [29] in solving the flow at Re = 150, concluded that the flow modification is due to mean flow alteration by the action of the divergence of Reynolds stress tensor that arises due to forcing. This can be construed as the modification at the zeroth mode of the nonlinear effects for the instability of the wake. Thiria *et al.* [19] concluded that the phase lag between the vortex shedding and the imposed rotary motion can contribute constructively to decrease fluctuations in the wake to cause net drag reduction.

Observed cases for Re = 150 in Thiria *et al.* [19] can be simulated by solving Navier- Stokes equation and detailed results would help understand the physical mechanisms for drag reduction by rotary oscillation at low Reynolds numbers. We have solved here the Navier-Stokes equation using the high-accuracy methods used in Sengupta *et al.* [30] and Dipankar *et al.* [31]. We also report results for Re = 1000 to investigate how the drag reduction mechanism alters with Reynolds number.

Williamson [32] noted that the flow past stationary cylinder remains two-dimensional for Re < 178. Dimensionality of the flow past a cylinder is often related to the shedding mode of vortices in the wake. A flow displaying oblique shedding is definitely three-dimensional, while the flow displaying parallel shedding can be two-dimensional at lower Reynolds number. Khalak & Williamson [33] have experimentally demonstrated that the mean drag of parallel and oblique shedding cases differ by nearly 15 to 20%, with the former showing higher values up to moderate Reynolds number. It is interesting to note that the experimental unsteady lift-force data compiled in Khalak & Williamson [33] from previous studies revealed a scatter of the order of 400%. The results in Poncet [34], [35] provide data for flow past a cylinder executing rotary oscillation that suggest the coherent forcing along the full-span precludes spanwise variation of flow in that direction. Three-dimensional effects arise due to flow instability and/ or end effects. This is also supported in Fig. 2 of Thiria *et al.* [19] showing flow visualization picture without any significant spanwise variation of the flow. Tokumaru & Dimotakis [17] also noted that the wake structure is strongly controlled by the strength and spacing of the shed vortices from the oscillating cylinder. These provide impetus to study flow past cylinder at higher

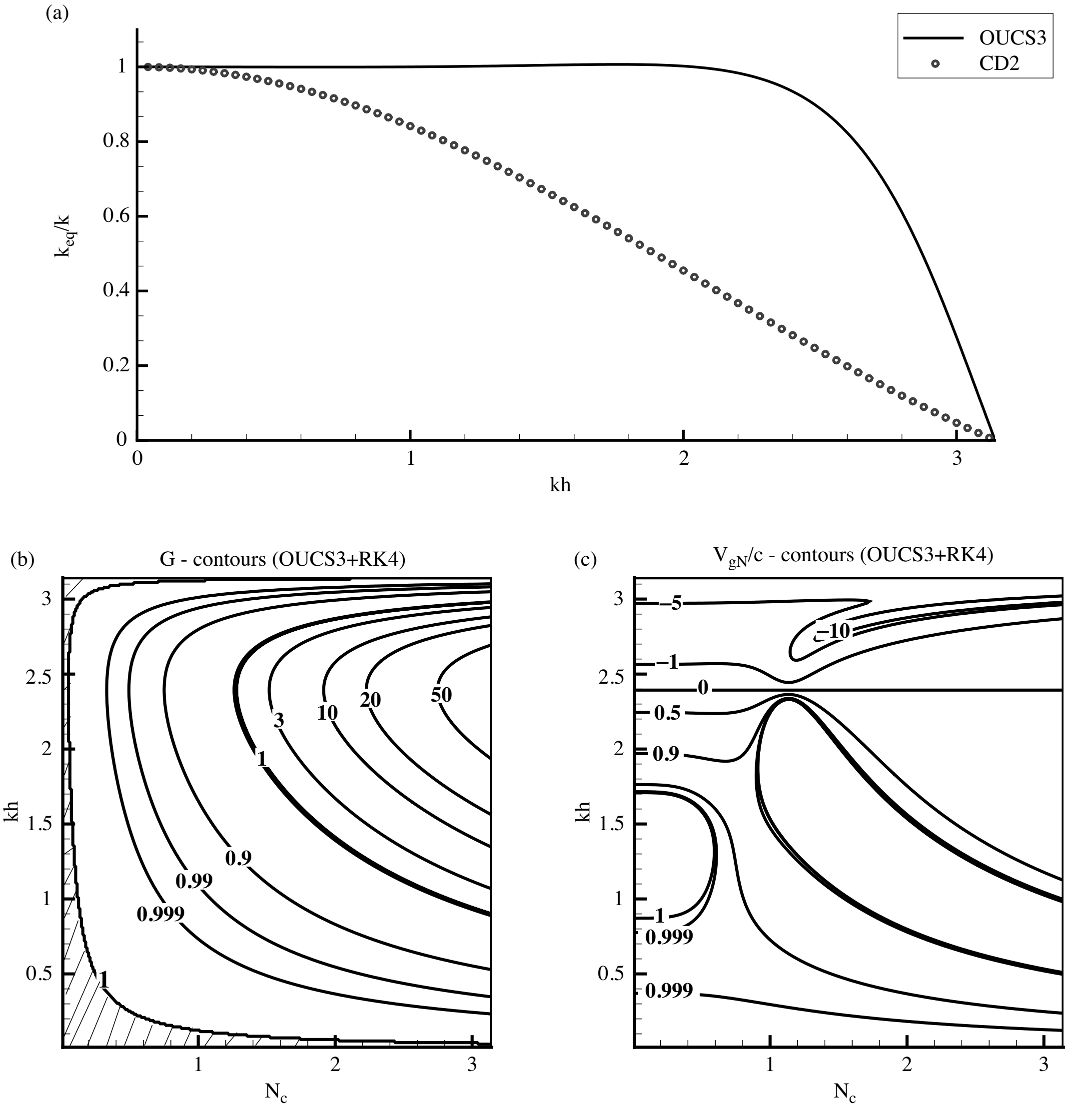

Fig. 2(a) Comparison of scale resolution between second order central difference scheme and the compact scheme used here. (b) The numerical amplification factor for the solution of 1D convection equation using the compact scheme and the four stage Runge-Kutta time integration scheme. (c) Normalised numerical group velocity contours for the solution of 1D convection equation using the same schemes as in (b).

Reynolds numbers with a two-dimensional flow model when the flow is controlled by rotary oscillation. Note that the simulations in Shiels & Leonard [26] and Sengupta *et al*. [11] were obtained using two-dimensional flow models for $Re = 15,000$. Present study is restricted up to $Re = 1000$, as in Choi *et al*. [23].

The agreement between actual flow field and two-dimensional simulation is due to the fact that bluff-body flows admit other routes of energy redistribution among different scales, other than the energy cascade by vortex stretching - a mechanism present only for three-dimensional flows. Here we study the bypass transition route, discussed earlier for two-dimensional flows in Sengupta *et al*. [27], Lim *et al*. [28] , Shiels & Leonard [26] . Shiels & Leonard [26] reported *boundary layer bursting leading to multi-pole vorticity structure* responsible for drag reduction. Such bursting phenomenon were also noted in Sengupta *et al*. [27] for vortex-induced instability problems. With rotary oscillation, the flow is dominated by the two-dimensional motion in the near-vicinity of the cylinder and a two-dimensional assumption is adequate for this flow as compared to the case of flow past a stationary cylinder.

2 GOVERNING EQUATIONS AND NUMERICAL METHOD

The two-dimensional Navier-Stokes equations in stream function-vorticity formulation are given in non-dimensional form as,

$$\nabla^2 \Psi = -\omega, \tag{2}$$

$$\frac{\partial \omega}{\partial t} + V . \nabla \omega = \frac{1}{Re} \nabla^2 \omega \tag{3}$$

Where ω is the out of plane component of vorticity and the velocity is related to the stream function by $V = \nabla \times \Psi$, where $\Psi = (0, 0, \Psi)$. The $(\Psi - \omega)$ formulation is preferred here due to its accuracy and efficiency in satisfying mass conservation exactly everywhere. The flow is computed in the transformed orthogonal grid $(\xi - \eta)$ plane. The transformed co-ordinate ξ is the scaled azimuthal co-ordinate, while η is the transformed, scaled radial co-ordinate. Additional details of the formulation used here can be found in Dipankar *et al*. [31].

The pressure field is obtained numerically by solving the governing pressure Poisson equation (PPE) for the total pressure p_t, given in the orthogonal coordinate system by,

$$\frac{\partial}{\partial \xi}\left(\frac{h_2}{h_1}\frac{\partial pt}{\partial \xi}\right) + \frac{\partial}{\partial \eta}\left(\frac{h_1}{h_2}\frac{\partial pt}{\partial \eta}\right) = \frac{\partial}{\partial \xi}(h_2 v\omega) - \frac{\partial}{\partial \eta}(h_1 u\omega) \tag{4}$$

Where h_1 and h_2 are the scale factors of the transformation given by,

$$h_1 = (x_\xi^2 + y_\xi^2)^{\frac{1}{2}} \text{and } h_2 = (x_\eta^2 + y_\eta^2)^{\frac{1}{2}}.$$

The no-slip boundary condition on the cylinder wall is satisfied by

$$\frac{\partial \Psi}{\partial \eta_{body}} = h_2 r_0 \Omega \tag{5}$$

where Ω is the non-dimensional value of the rotary oscillation defined in equation (1). Additional condition arising out of no-slip condition is given by

$$\Psi = constant. \tag{6}$$

This condition is used to solve the Poisson equation for the stream function equation (2), while both the equations (5) and (6) are used to evaluate the wall vorticity ω_b that provides the boundary conditions for the vorticity transport equation (VTE) given by equation (3).

At the outer boundary, uniform flow condition is applied for the inflow (Dirichlet condition on ψ) and convective boundary condition on radial velocity at the outflow is applied, as shown in Fig. 1. The radiative condition or the Sommerfeld boundary condition applied (in the sector QR) at the outflow is as given in Esposito *et al*. [36], Orlanski [37] and given by,

$$\frac{\partial u_r}{\partial t} + u_c(t)\frac{\partial u_r}{\partial r} = 0, \tag{7}$$

Where u_r is the radial component of velocity and $u_c(t)$ is the convection velocity at the outflow at time t, which is obtained from the radial component of velocity at the previous time step, i.e., $u_c(t) = u_r(t - \Delta t)$. It is not very important where Q and R in Fig. 1 are located in fixing the outflow, but adequate care is exercised to prevent numerical problem arising out of the mismatch between the Dirichlet condition in the inflow and the radiative condition at the outflow.

The initial condition is given by an impulsive start of the cylinder in a fluid at rest. The vorticity on the outer boundary is obtained by using the kinematic definition of vorticity, as given in equation (2). Poisson equations are solved using the Bi-CGSTAB variant of the conjugate gradient method of Van der Vorst [38]. The Bi-CGSTAB method is made to converge faster by using ILUT pre-conditioners as described in Saad [39]. To solve the PPE, the required Neumann boundary condition on the physical surface and in the far-field are obtained from the normal (η) momentum equation given by,

$$\frac{h_2}{h_1}\frac{\partial p}{\partial \eta} = -h_1\ u\omega + \frac{1}{Re}\ \frac{\partial \omega}{\partial \xi} - h_1\frac{\partial \upsilon}{\partial t} \tag{8}$$

The convection terms in (3) and (8) are evaluated using compact scheme, those are implicitly evaluated and provide a spectral-like accuracy. Use of compact schemes allow the solution of the Navier-Stokes equation for the rotary oscillation case which were otherwise not possible for moderate Reynolds number flow by lower accuracy methods. The particular compact scheme used here is compared with other discretization methods in Sengupta *et al.* [30],[40].

3 RESULTS AND DISCUSSION

Here, attention is focused only on flow past a circular cylinder executing rotary oscillation for $Re = 150$ and 1000. The instantaneous vorticity contours shown in Fig. 1, correspond to the case of $A = 2$ and $f_f/f_0 = 3$ for $Re = 150$. First, we discuss about the numerical method and its validation with respect to available experimental and other computational results for similar flows.

The numerical methods used here are those described in Sengupta *et al.* [11], Dipankar *et al.* [31]. We only highlight the properties of the high accuracy compact scheme, OUCS3 used to discretize convection terms of the VTE. If a variable is defined by its Laplace transform, $u(x, t) = \int U(k, t)e^{ikx}\, dk$, then its exact spatial derivative is $\left(\frac{\partial u}{\partial x}\right)_{ex} = \int ikU(k, t)e^{ikx}dk$. When this derivative is obtained numerically, it can be written equivalently as $\left(\frac{\partial u}{\partial x}\right)_{num} = \int ik_{eq}U(k, t)e^{ikx}dk$. In Fig. 2(a), the present method is compared with the second order accurate central difference scheme (CD2), showing k_{eq}/k (a measure of scale resolution), is plotted against kh, with h representing the uniform grid spacing used. Ideally, k_{eq}/k should be equal to one, but all discrete methods filter length scales by different amount- as shown in this figure. The CD2 scheme can compute the first derivative accurately for a very small range of kh, as compared to the OUCS3 method that resolves the derivative up to $kh = 2.3$- an order of magnitude improvement over CD2 method.

Apart from the scale resolution property, one must also check for the numerical stability and dispersion property for the direct simulation of space-time dependent problems. The numerical stability is defined by the numerical amplification factor $G(k, \Delta t) = U(k, t + \Delta t)/U(k, t)$ that should also ideally be equal to one, for $\Delta t \to 0$. A parameter that indicates the time step, is the Courant-Friedrich Lewy (CFL) number $N_c = c\Delta t/U_\infty$, with c a convection speed at which the phase of the variable changes. In Fig. 2(b), the G contours are shown plotted in $(kh - N_c)$-plane for the solution of one-dimensional convection equation. The G-contour has the desirable neutral stability retained across the resolved length scales for a small range of N_c values, shown by the hatched region in the figure. The other important property of any numerical method relates to preserving the actual physical dispersion relation. This is the dispersion relation preservation (DRP) property [30], given by the numerical group velocity (Vg_N) of the method. For the one dimensional convection equation, this is displayed by V_{gN}/c, plotted in the $(kh - N_c)$-plane in Fig. 2(c). Here, the OUCS3 method retains the DRP property effectively for low values of N_c as compared to CD2 method. In Fig. 2(c), we are restricted to keep kh below 2.4, otherwise the computed vortical structures go in the opposite direction. For CD2 method, such a limit is given by $kh = 1.578$.

All computations are performed using an orthogonal grid of size (150×450), with 150 points in the azimuthal direction and 450 points in the radial direction. Points in the azimuthal direction are spaced at equal angular intervals. In the radial direction, points are distributed non-uniformly [11], with the first point at a distance $0.001d$ from the surface of the cylinder and the outer boundary is located at $20d$ from the centre of the cylinder. Solutions of (3) and (4) provide the vorticity and total pressure, respectively in the flow field. The surface pressure is readily obtained from the total pressure to calculate the drag acting on the cylinder at any instant by performing the following contour integral over the surface of the cylinder,

$$Cd = \frac{2}{d}\int_{cyl} (pn_x - T_{ix}\eta_i)dl \tag{9}$$

Where p is the surface pressure and τ_{ix} is the viscous stress on the surface of the cylinder with η_i as the unit normal vector in the i^{th} direction. In this paper, we refer the instantaneous drag coefficient by C_d, whereas its time-averaged value is indicated by C_D. In reporting the time averages, we have taken the time-series over a large integral number of cycles of the variables, after the transient effects have died down. Similarly, one obtains the lift and the pitching moment coefficients.

We provide validation of the method with respect to the results given in Henderson [41]. Flow over a stationary cylinder has been obtained to check C_D for Re = 150 and 1000. Fig. 3(a) shows a comparison of numerically obtained C_D with available experimental and computational results given in Henderson [41]. Our computed data are shown by solid square symbols for Re = 150 and 1000 and the solid line represents the computed results by Henderson solving Navier-Stokes equation. The data at Re = 1000 with a '+' symbol represents the three-dimensional simulation results of Henderson [41], while the rest of the discrete data are experimentally obtained. At Re = 150, very good match is obtained for our results with the experimental value and the computed results by Henderson [41]. For Re = 1000, our computed C_D is closer to the three-dimensional computations of Henderson [41], but both of them are different from the experimental value, as expected due to the three-dimensional nature of the flow in the experiments. We have already noted that with rotary oscillation of the cylinder, the flow will display two-dimensionality at higher Reynolds numbers, as compared to stationary cylinder case.

Further validation of the present method for rotary oscillation case is shown by comparing with experimental results in Thiria *et al.* [19] at Re = 150 for different A and f_f/f_0 values. The non-dimensional amplitude A and frequency ratio f_f/f_0 in Thiria *et al.* [19] are related to Ω_1 and S_f as $\Omega_1 = 2A$ and $S_f = 0.5131263 f_f/f_0$. For validation, apart from checking C_D variation with A, it is important to ensure that each and every resolved scales propagate their energy at the correct speed- the physical group velocity. For this reason, we have compared the numerical and physical group velocity in Fig. 2(b). Fig. 3(b) and 3(c) show comparison between numerically and experimentally obtained vortical structures from Thiria *et al.*, [19] over half the time period of rotary oscillation for the cases of $A = 2$; $f_f/f_0 = 1.5$ and $A = 2$, $f_f/f_0 = 3.0$ for Re = 150. In Thiria *et al.* [19], the flow field has been visualized using laser induced fluorescence technique, with the fluorescein dye injected on both side of the centerline of the tunnel upstream of the cylinder. The dye was illuminated by an argon ion laser and if the non-conservative source strength of fluorocein is negligible then the tracer material follows the flow. The dye would be trapped in the flow where it stagnates due to low convection speed and would reveal the vortices in the

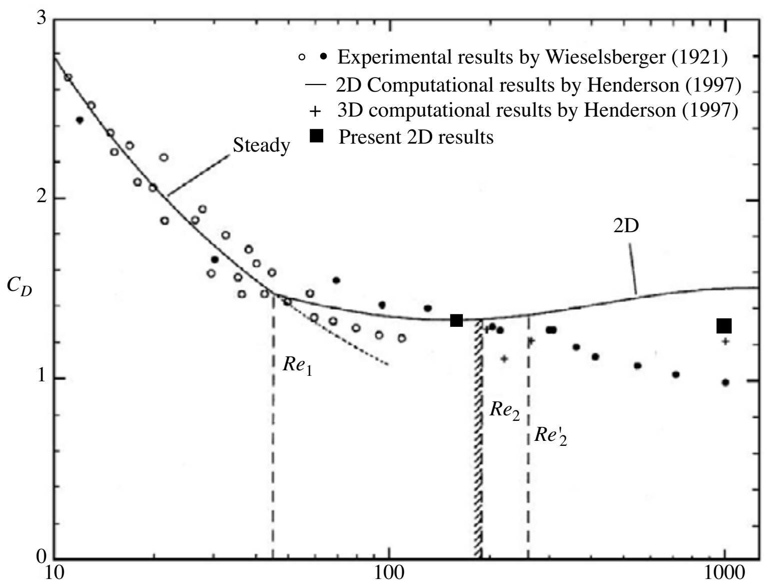

Fig. 3 (a). Comparison of the numerically obtained drag coefficient for the flow around a stationary circular cylinder with numerical and experimental results given in Henderson [41].

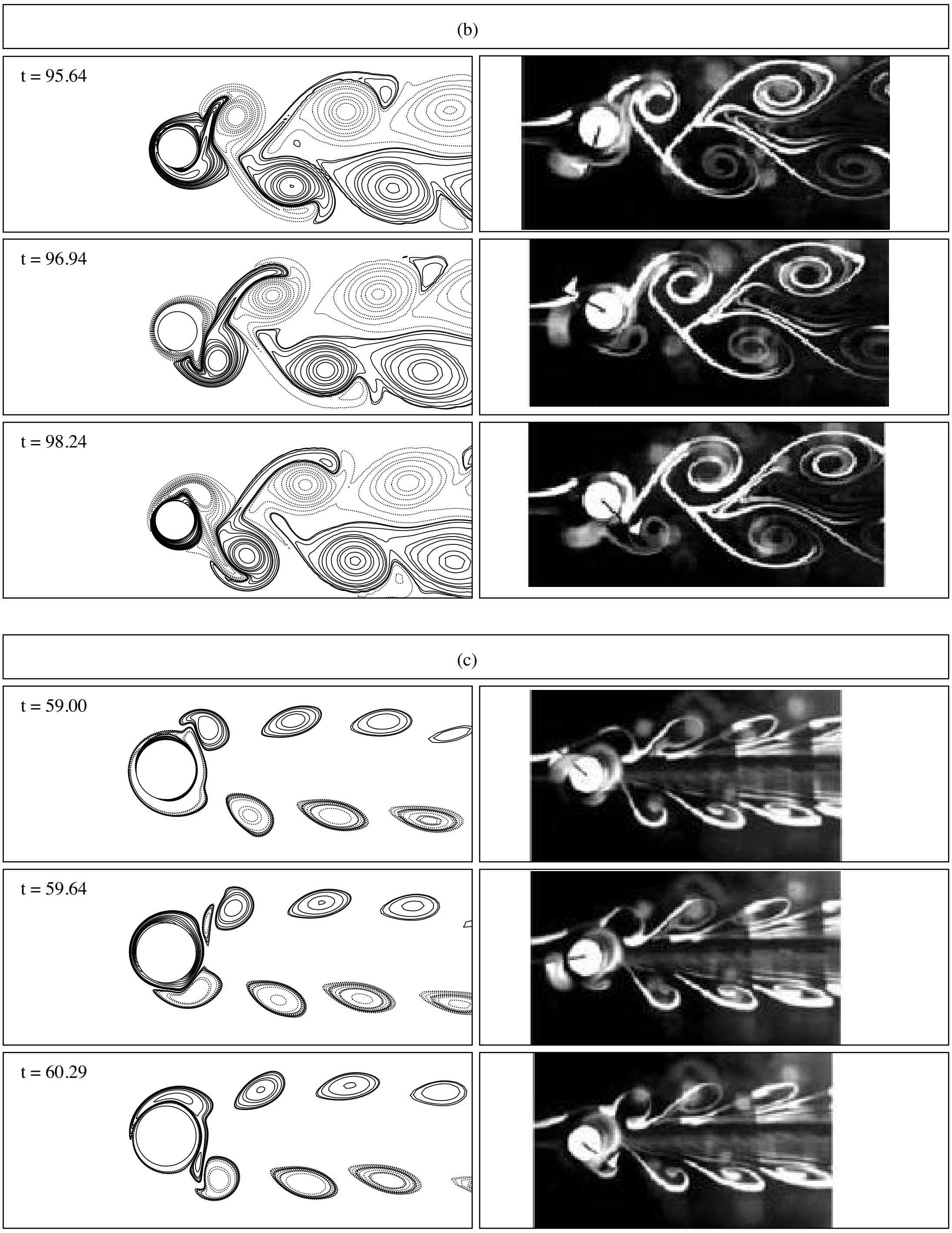

Fig. 3. (b) Comparison of computational vorticity contours and experimental flow field (Thiria et al., [19]) around a cylinder executing rotary oscillation for a case of Re = 150, A = 2 and f_f/f_0 = 1.5 in equation (1) defining the rotary oscillation. (c) Comparison of computational vorticity contours and experimental flow field (Thiria et. al., [19]) around a cylinder executing rotary oscillation for a case of Re = 150, A = 2 and f_f/f_0 = 3.0 in equation (1) defining the rotary oscillation.

wake clearly. This is the reason that the computed vorticity contours match with the visualization of the experiment.

To capture the vortical structures more accurately, the computations for Fig. 3(b) used a (250×600) -grid with a time step of $\Delta t = 4 \times 10^{-5}$. One can clearly observe different length scales of the experiment completely resolved in the computation. Growth and movement of the vortical structures towards the

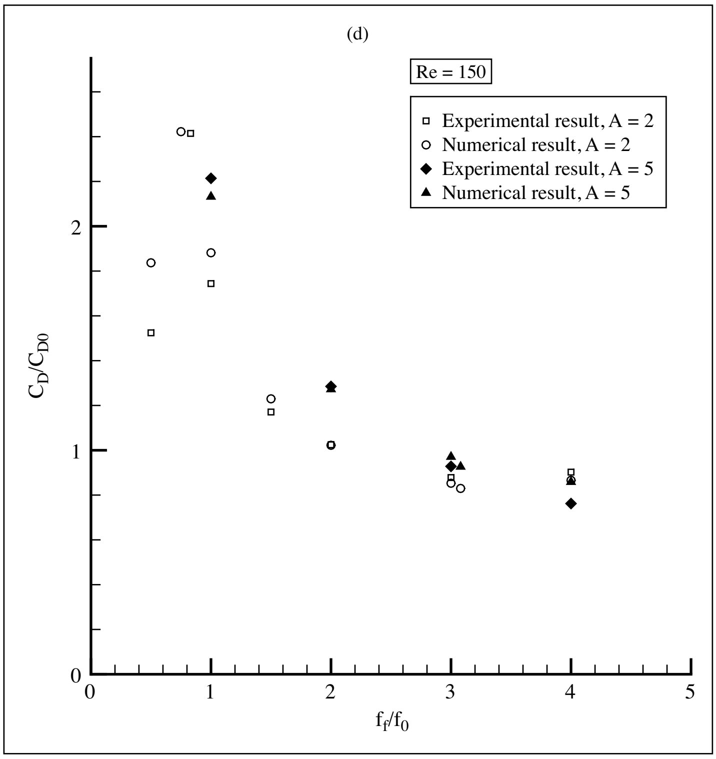

Fig. 3(d). Comparison of the numerical and experimental (Thiria et al., [19]) normalised time-averaged drag coefficient values at different frequencies for the cases, A = 2 and A = 5.

outflow in computations are exactly identical to that seen in the flow visualization picture. For the computed results shown in Fig. 3(c), we have used a further refined (400 × 500) grid with the time step of $\Delta t = 4 \times 10^{-5}$ to establish grid independence of the computed solutions. In this case, the rotational frequency of the cylinder is doubled with respect to the previous case and one can see two parallel streets of vortices, completely resolved in the simulation.

Quantitative comparison and validation is provided in Fig. 3(d) showing variation of C_D/C_{D0} with f_f/f_0 at the constant amplitudes of $A = 2$ and 5. C_{D0} is the time-averaged drag coefficient for the unforced case at $Re = 150$. The computed results match excellently with the experimental results from Thiria *et al.* [19]. However, for f_f lower than f_0, the numerical results deviate slightly from the experimental values. For $A = 5$ the match between the experimental and computational drag values for all f_f/f_0.

3.1 Effect of Forcing Frequency on Flow Control

It has been noted in [19] that the vorticity dynamics changes significantly for the cases with $f_f/f_0 > 1$ from the cases for $f_f/f_0 < 1$, for lower values of A. Here also, the same trend is captured for $A = 2$ case. To ascertain the same, in Fig. 4 results for $A = 0.5$ are shown for $Re = 150$ and 1000. The features of results for $Re = 1000$ are different from $Re = 150$ case- indicating a strong dependence on Reynolds number for low values of A. This has also been shown in Choi *et al.* [23], who reported results for $Re = 100$ and 1000. The minimum drag for $Re = 150$ occurs over a large range of frequency ratio, exhibiting very small drag reduction. As also noted [19], there occurs a drag maximum at lower frequency ratio that increases with A. This drag amplification is not due to resonant forcing and the detuning is amplitude dependent. For $A = 0.5$, appreciable drag reduction is not visible for $Re = 150$ and drag amplification occurs the most for $f_f/f_0 = 1.0$. For $Re = 1000$ and $A = 0.5$ about 10 to 15% drag reduction is noted for a range of f_f/f_0. In Fig. 4, the drag actually increases once again above $f_f/f_0 = 4.0$ for $Re = 1000$, as compared to the cases shown for $Re = 150$. Reasons for this behavior are explored in section 3.5 using POD analysis.

3.2 Effects of Amplitude on Flow Control

For this study, we have focused our attention for the forcing frequency given by $f_f/f_0 = 3.06$. For this forcing frequency, direction of rotation alters after every time interval of $\Delta t = 1$. The region beyond

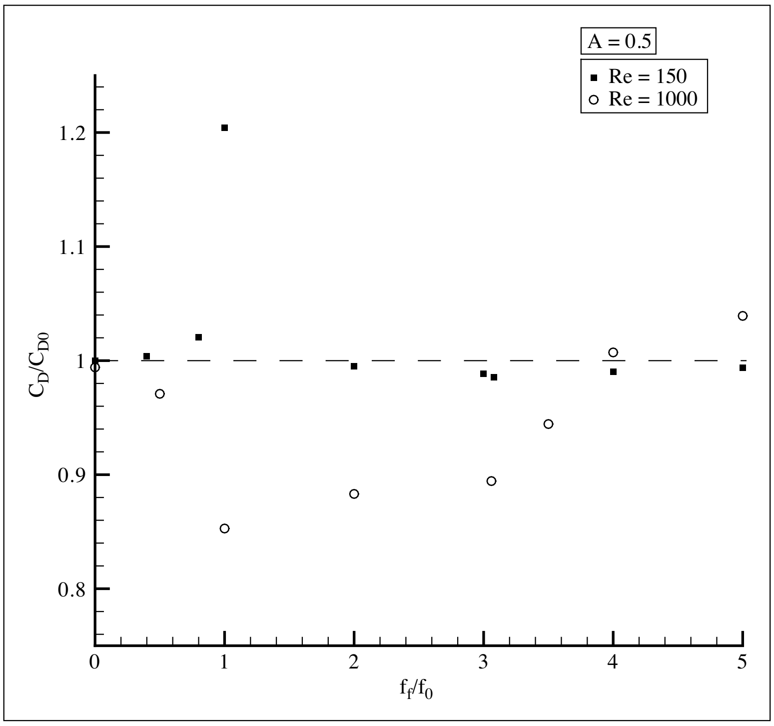

Fig. 4. Variation of normalised time-averaged drag coefficient for the indicated Reynolds numbers for a low amplitude of excitation (A = 0.5). Note the opposite behaviour of the drag coefficient for $f_f/f_0 = 1.0$.

which the vortices are eventually shed has been termed as the "lock-in" length [19]. In Fig. 5 vorticity contours are shown for different A at the fixed time of $t = 100$ to indicate that the "lock-in" length grows with A. To accommodate varying "lock-in" length, the computational domain is increased to *50d* for all the cases shown in this figure using a (150 × 500) grid. The first radial grid line is at a distance of $0.002d$ from the cylinder surface and the time step chosen is $\Delta t = 8 \times 10^{-5}$.

For the case of $A = 0.5$, the wake behind the cylinder resembles the wake of a stationary cylinder. However near the surface of the cylinder, formation of separating shear layer is strongly dominated by the rotary oscillation. Separation is promoted in an unsteady manner by the rotary oscillation on that part of the cylinder where the rotary motion creates an upstream motion deep inside the wall boundary layer. This promotes the formation of what has been termed as flapping vortices in Thiria *et al*. [19], the same is also noted here as small scale vortices those flap around the cylinder before being stripped away periodically.

At smaller values of $A = 0.5$ and 1.0, the small scale vortices retain their size and do not elongate. So vortex stripping mechanism is weaker at lower values of A. For $A \geq 1.5$, one can observe a pair of small vortices forming immediately behind the cylinder (marked as A_1B_1 in the frame for $A = 1.5$) those grow in radial direction and larger vortices form at the edge of A_1B_1 that appear as the vortex street, with significantly lower streamwise distance between the successive vortices. This is a typical structure of vortices within the "lock-in" length. In the far wake - beyond $x/d = 7.5$- the shed vortices for $A = 2$ appear as regular shed vortices for stationary cylinder case. Due to the flapping vortices and the vortex stripping mechanism a broad spectrum of scales are generated in the flow. With increase in amplitude, the "lock-in" length increases slowly up to $A = 2$. Beyond the "lock-in" length, alternate shedding of vortices is due to transition from absolute to convective instability of the flow field. With further increase of A, this transition weakens and between $A = 2$ and 2.5, there is a sudden growth in the "lock-in" length. This growth is continued up to $A = 4$, where the "lock-in" length covers the complete length of the computational domain. Distinct weaker vortical structures noted in this frame remain interconnected without any relative motion. Above this value, the "lock-in" length again decreases, as noted for $A = 5$. Next, we identify the scales and frequencies of the flow with change in amplitudes from the integrated loads and their spectra.

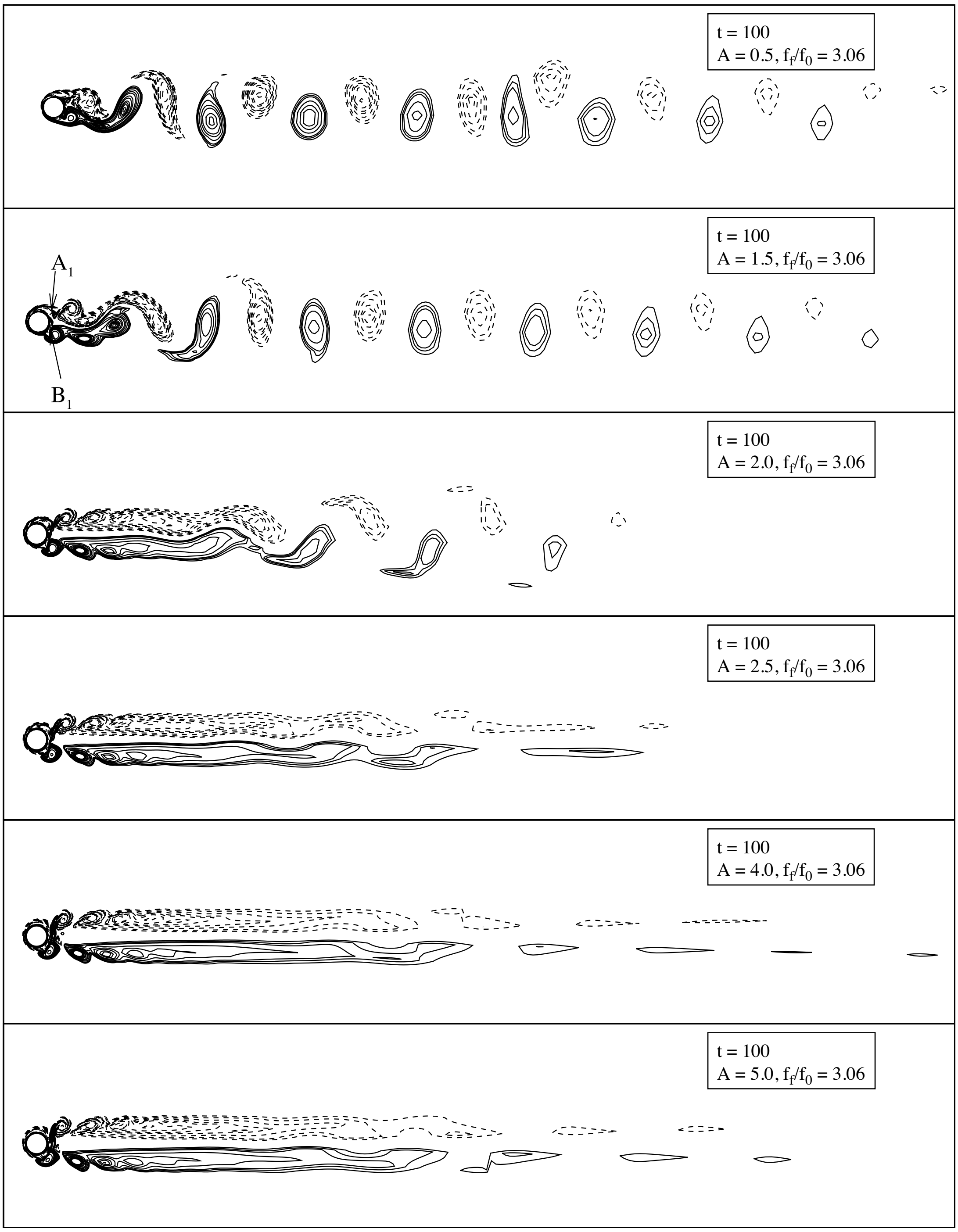

Fig. 5. Computed vorticity contours at t = 100 for the case of Re = 150 and f_f/f_0 = 3.06 for the indicated amplitudes of excitation.

3.2.1 Loads and Spectra

In Fig. 6(a), the variation of C_d is shown for the different amplitude cases for $Re = 150$ and $f_f/f_0 = 3.06$ on the left column, along with their FFT on the right column. The unforced case is also included on the top frames for reference. When the rotary oscillation is applied, C_d plots show irregular time variation presence with multiple discrete frequencies present- as seen from the FFT. As also the amplitude is defined by $A = V_{max}/U_\infty$, the case of $A = 1$ indicates that a part of the cylinder surface motion is in-phase with the free stream that releases shear locally. Simultaneously, another part of the surface experiences enhanced shear where the relative velocity is maximum. Any value of $A \neq 1$, will introduce multiple time intervals when flow will change signs. This in essence introduces additional time scales, as seen

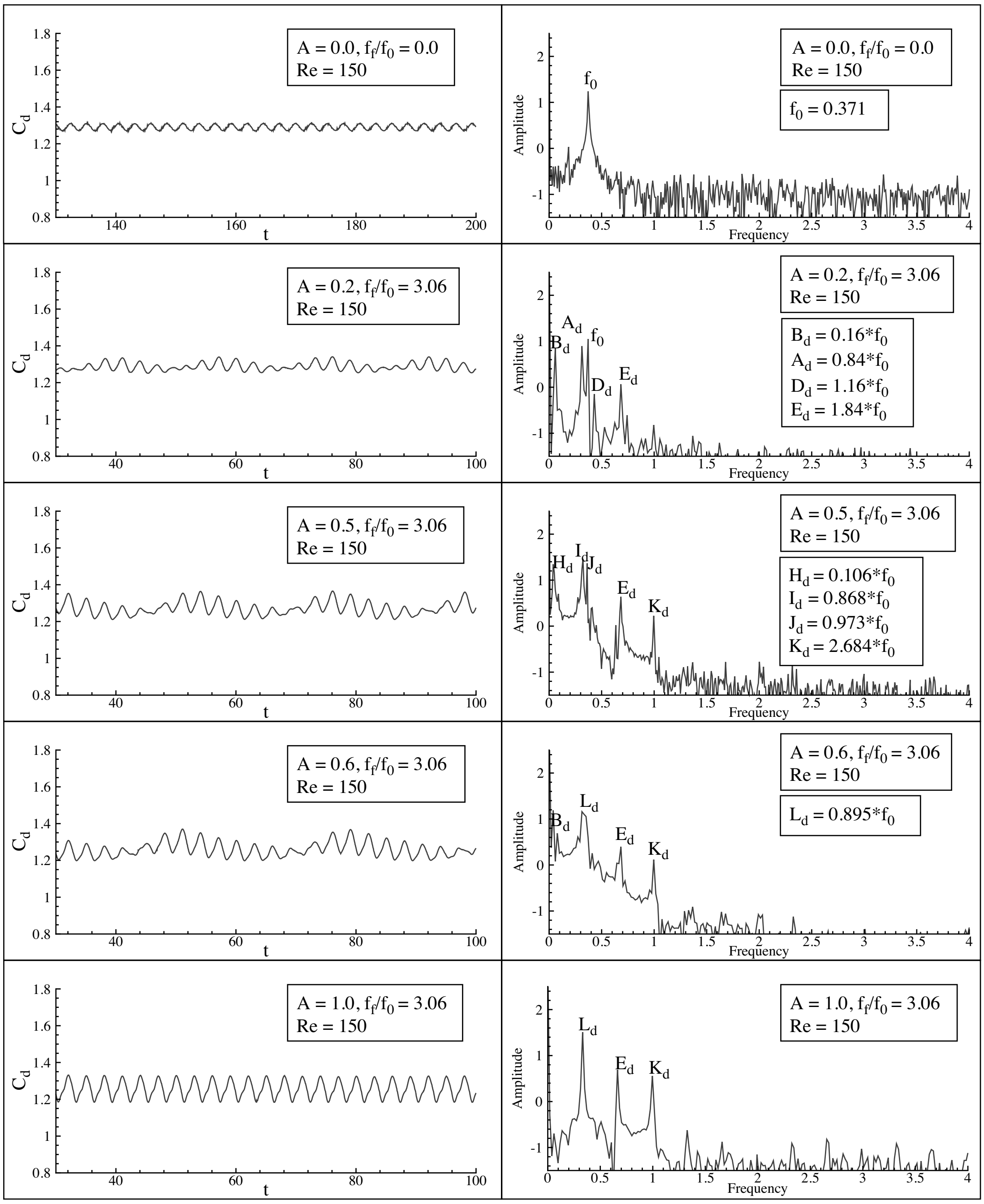

Fig. 6(a). Drag coefficient variation with time (left) and it's Fourier transform (right) for the case of Re = 150 and f_f/f_0 = 3.06 for indicated amplitude of rotary oscillation. Here the amplitudes are in logarithmic scale. The major frequencies have been identified for different amplitude of excitation. The top frames are for the case of stationary cylinder. (Cont.)

in the load history and its spectrum. For values of $A << 1$, the weaker flapping vortices cause a larger vertical sloshing of the shed vortices from a shorter "lock-in" length that is responsible for largest drag, which has been noted and termed as drag amplification in Thiria *et al*. [19]. The presence of discrete frequencies as seen in the FFT has been identified to cause alterations in mean flow via fluctuations in [29], [19]. The results in Fig. 6(a), however, indicate that these fluctuations themselves change with the variation of A. For example, between $A = 1.8$ and 2.0, C_d variation shows a *transitional* behavior, with the subharmonics progressively disappear. This absence of multi-periodic behavior is the root cause of largest drag reduction for this range of amplitude. It is equally interesting to note that there is only a single peak, as is seen also in the unforced case. However, the peak amplitude is smaller for the optimal

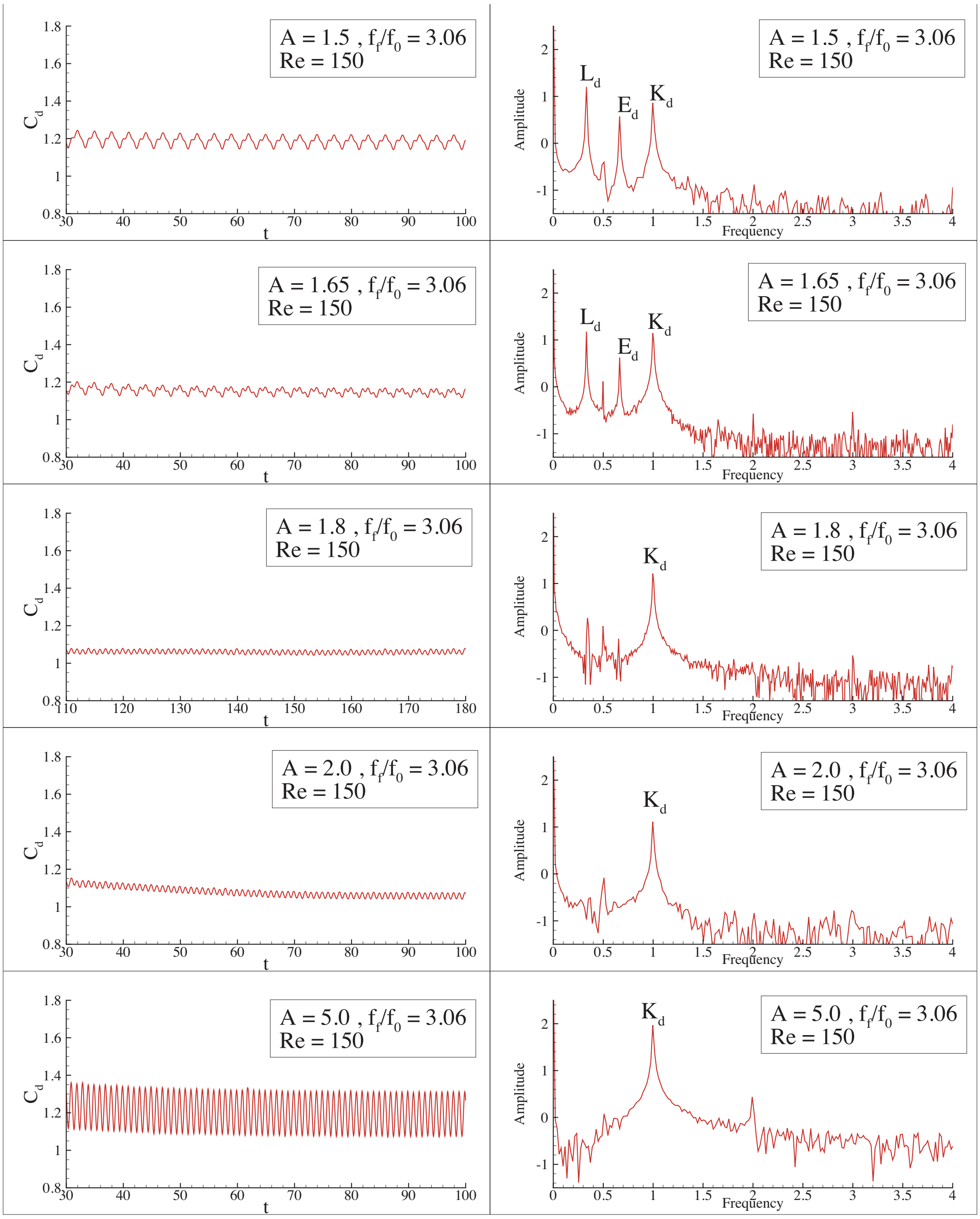

Fig. 6(a). Drag coefficient variation with time (left) and it's Fourier transform (right) for the case of Re = 150 and f_f/f_0 = 3.06 for indicated amplitude of rotary oscillation. The amplitudes are in logarithmic scale. The major frequencies have been identified for different amplitude of excitation.

control case, as compared to the unforced case. Above A = 2.0 one notices increased fluctuating component at all higher frequencies, that accounts for increased drag.

Appreciation of events in the wake can be obtained further from the Fourier transform of the loads. In the unforced case, there is only one dominant peak located at $f_0 = 0.371$. When the cylinder executes rotary oscillation at low amplitude, newer frequencies appear - as seen from the FFT for A = 0.2. Distinct peaks at B_d, $A_d = (f_0 - B_d)$, $D_d = (f_0 + B_d)$ and $E_d = (f_f - f_0 - B_d)$ are noted for this case. When A is increased to 0.5, the peaks are at shifted frequencies. The peak at A_d interacts with f_0 to give rise to I_d and J_d, the difference of these two new frequencies appears as the peak at $H_d = J_d - I_d$. With further increase in A, E_d retains its presence while a new time scale appears that has permanent presence with change in A. This peak at K_d is seen as the combination $K_d = E_d + (J_d + I_d)/2$. The combination of $L_d = (J_d + I_d)/2$ is also present in subsequent frames for $A \geq 0.6$. This coalescence of J_d and I_d into L_d also removes the very low frequency beat noted corresponding to H_d. The events at L_d and E_d can be viewed as sub-harmonic excitation of the events at K_d. These three frequencies continue to dominate the time variation for $0.8 \leq A \leq 1.5$- above this we note significant drag reduction. It implies that the global drag minimum is achieved by the removal of the sub-harmonic excitation of scales, while their presence can lead to sub-optimal drag reduction. The cases with $A \leq 0.8$ are richer in frequency than the higher amplitude cases. As A increases, amplitude of events at the frequencies L_d and E_d comes down and they are seen to be absent for $A \geq 1.8$, while the amplitude at K_d increases. Strengthening of K_d for $A > 2$ is the cause for drag increase beyond the global minimum.

In Fig. 6(b), the variation of C_l with time and its FFT are shown for few cases. The unforced case shows mainly periodic variation of C_l at Strouhal frequency, with significantly higher frequency fluctuations as well. The lower A cases (not shown here) display two changes: (i) the disappearance of high frequency fluctuations and (ii) the appearance of lower frequency multi-periodic time variation of lift. Both of these changes are consequences of coherent forcing. This also testifies the assertions by previous authors that

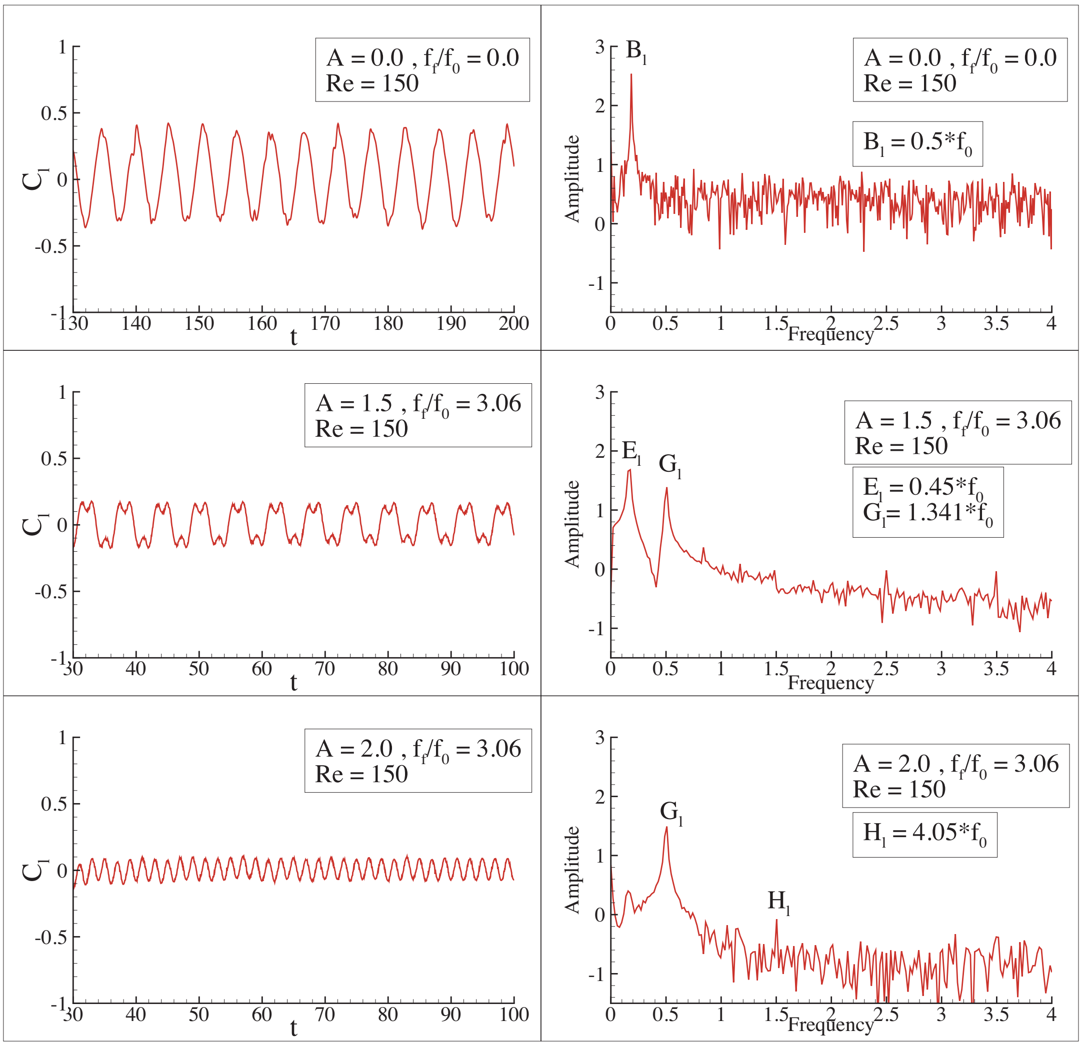

Fig. 6(b). Lift coefficient variation with time (left) and its Fourier transform (right) for the case of Re = 150 and $f_f/f_0 = 3.06$ for the indicated amplitudes of rotary oscillation. Here amplitudes are in logarithmic scale. The major frequencies have been identified for different cases. The top frames are for the case of a stationary cylinder.

the forcing enhances two-dimensionality for the controlled flow. Similar to C_d variation, here also the peak-to-peak variation of lift reduces with the amplitude of oscillation up to $A = 2.0$. In the unforced case, there is the dominant frequency at $B_l = f_0/2$. For $A = 1.5$, two peaks appear, one at the frequency $G_l = 1.341f_0$- which is also exactly equal to half the value of the frequency at K_d in Fig. 6(a) and another at $E_l = 0.45f_0$. As we increase amplitude further, the frequency G_l remains dominant in the flow, with another peak at H_l (the forcing frequency) continues to strengthen, but remain sub-dominant.

Fig. 6(c) shows C_D/C_{D0} variation with the forcing amplitude (A) for $f_f/f_0 = 3.06$. As shown here, rotary oscillation at this frequency results in drag reduction for all the amplitude cases. As A increases from

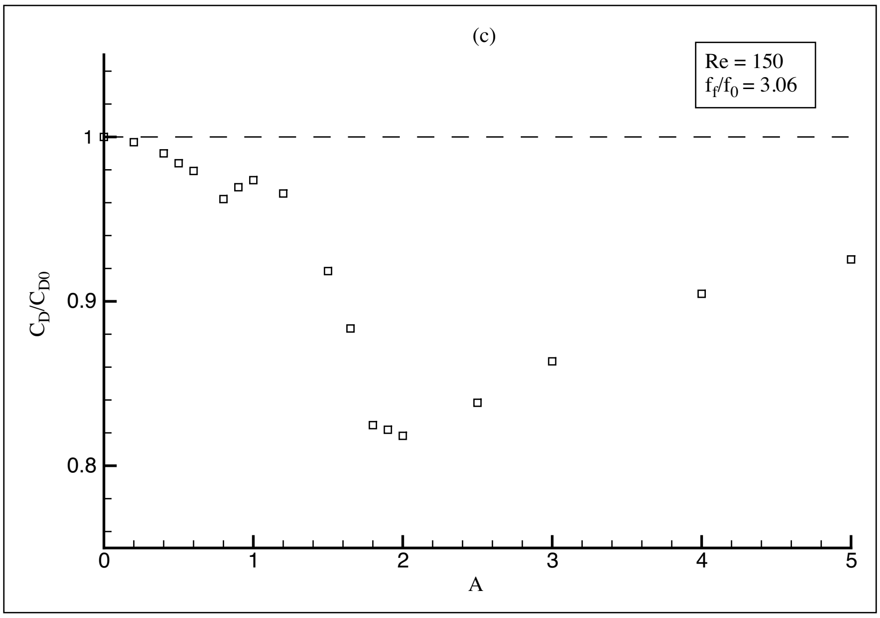

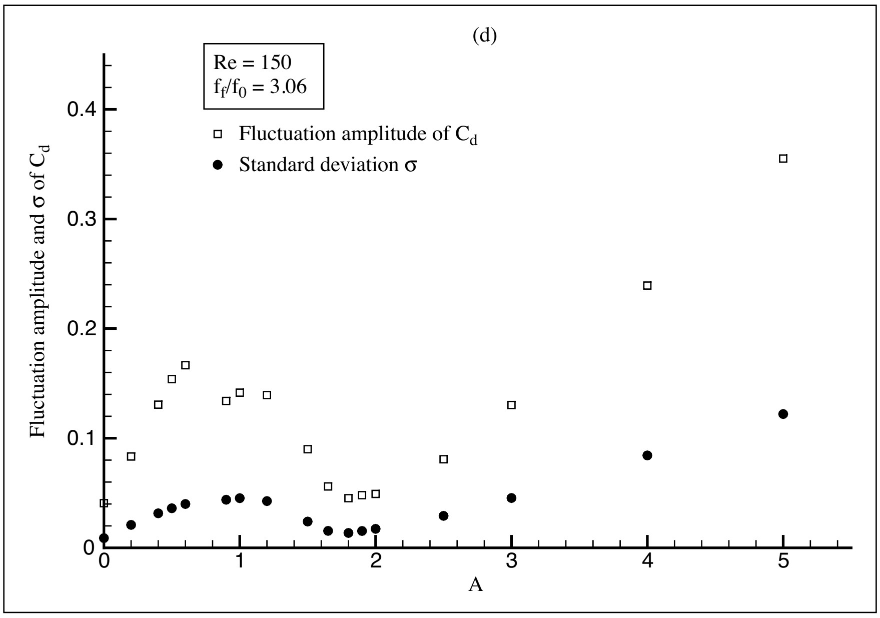

Fig. 6(c) Normalised drag coefficient variation with amplitude of rotary oscillation for the case of Re = 150 and $f_f/f_0 = 3.06$. Note the presence of local minimum in addition to the global minimum for the drag coefficient. (d) Variation of fluctuating drag coefficient (peak-to-peak amplitude) and standard deviation σ of the drag coefficient with amplitude of rotary oscillation for the case of Re = 150 and $f_f/f_0 = 3.06$. Here also one notices a local minimum in addition to the global minimum.

0 to 2, there is a sharp fall in C_D, followed by the monotonic increase in C_D/C_{D0} as A is increased up to 5. This is caused by the following sequence. For low values of A, C_D is mainly dictated by the wake-width- typical of bluff-body flows. This is noted from the vorticity contour-plots of Fig. 5, for which the lower amplitude cases show wake structure similar to vorticity pattern for stationary cylinder. Width of the wake reduces as we increase A up to 2, and above $A = 2$, we have noted that the "lock-in" length increases forming narrow parallel vortex streets with lower pressure drag, while the drag due to viscous losses keeps increasing with A. With increase in A, the "lock-in" length and drag also increases monotonically up to $A = 5$. In Fig. 6(d), the peak-to-peak variation of C_d and its standard deviation are shown with A. The peak-to-peak variation and its standard deviation show similar trend with two local maxima before $A = 2$. At $A = 2$ the fluctuations are the least, while both these quantities show monotonic increase thereafter.

The flow behavior displayed for $Re = 150$ is quite revealing about the ways various control parameters determine the flow. One of the major parameter being the Reynolds number, its effect is studied in the next subsection for $Re = 1000$ and compared with results for $Re = 150$ for different forcing frequencies.

3.3 Effects of Frequency and Reynolds Number on Loads

Here, effects of variation of frequency are studied for $Re = 150$ and 1000 by plotting drag coefficient in Fig. 7(a) as a function of time, for the case of $A = 0.5$. One notes that the unexcited case latches on to the natural mode via growth of background disturbances. Because of the smallness of such background disturbances in a computational framework, it takes a while for the system to display visible natural periodic mode. However with a definative finite excitation imposed by rotary oscillation the fluid dynamical system latches quickly on to the natural periodic mode as compared to the unexcited case. For $f_f/f_0 = 1.0$, one can see that the higher Reynolds number case has significantly lower drag as compared to the uncontrolled case, while for $Re = 150$, the drag actually increases as compared to the uncontrolled case. The drag reduction for $Re = 1000$ is of the order of 15%, while for $Re = 150$ the drag coefficient actually increases by more than 20%, as was also shown in Fig. 4. For $f_f/f_0 = 2$, both the Reynolds number cases show the drag to reduce as opposed to the $f_f/f_0 = 1$ case. Here, the drag reduction is more than 10% for $Re = 1000$, while the drag reduction is marginal for $Re = 150$ case. For $Re = 1000$, computations have been performed up to $t = 250$ to obtain the time averages shown in Fig. 4. We note that the controlled cases for $Re = 1000$ display large amplitude, low frequency fluctuations for f_f/f_0 up to 3.06, that disappears for higher frequency excitations.

In Fig. 7(b), the Fourier transforms of C_d are compared for $Re = 150$ and 1000 cases. Discrete frequencies of importance in the spectra are marked and their values are identified in the frames. From the C_d data for both the Reynolds number, one can notice low frequency fluctuations- as noted from the time series in Fig. 7(a). These low frequency oscillations are due to interactions of f_0 and a neighboring frequency at E, H and K for $f_f/f_0 = 2$, 3.06 and 4, respectively. Additionally for $f_f/f_0 = 4$, the event at J is due to interaction between K and L. The low Reynolds number cases are characterized by fewer discrete frequencies, while for $Re = 1000$, the spectrum is continuous for lower frequencies of excitation. For $Re = 1000$ with $f_f/f_0 = 4$, one notices distinct peaks in Fig. 7(b) and there also we see interactions among different discrete frequencies.

3.4 Effect of Amplitude of Oscillation on Load for Re = 1000

To investigate effects of low amplitude excitations, we have simulated cases of $f_f/f_0 = 3.06$ for $Re = 1000$ and $A \leq 1$. The time series for drag coefficient are shown in Fig. 8(a), for the indicated values of A. All the three controlled cases display a lowering of the drag value, as compared to the uncontrolled value $C_D = 1.2829$. Computed C_D for the three controlled cases for $A = 0.25$, 0.50 and 1.00 are obtained as 1.273, 1.165 and 0.8590, respectively, indicating the drag to keep falling with increase in A. Further insight is obtained from the FFT of the time series of C_d for the above cases. In Fig. 8(b), the spectrum for the drag coefficient of the uncontrolled case shows one difference for $Re = 1000$ as compared to the value for $Re = 150$ case shown in Fig. 6(a), namely the appearance of a second peak in the FFT at f_0 (shown as B for $A = 0$). For the lower Reynolds number case, this was absent and its presence for $Re = 1000$ imply the role of non-linearity at higher Reynolds number originating from the convection terms of Navier-Stokes equation. With the application of rotary oscillation, one observes the appearance of more peaks in Fig. 8(b) for $A = 0.25$ and 0.50, at incommensurate frequencies. However, for $A = 1$, we note the peaks to be various sub- and super-harmonics of the fundamental. This once again reveals the special feature of $A = 1$ case for higher drag reduction that was discussed for $Re = 150$ case in Fig. 6(a), where

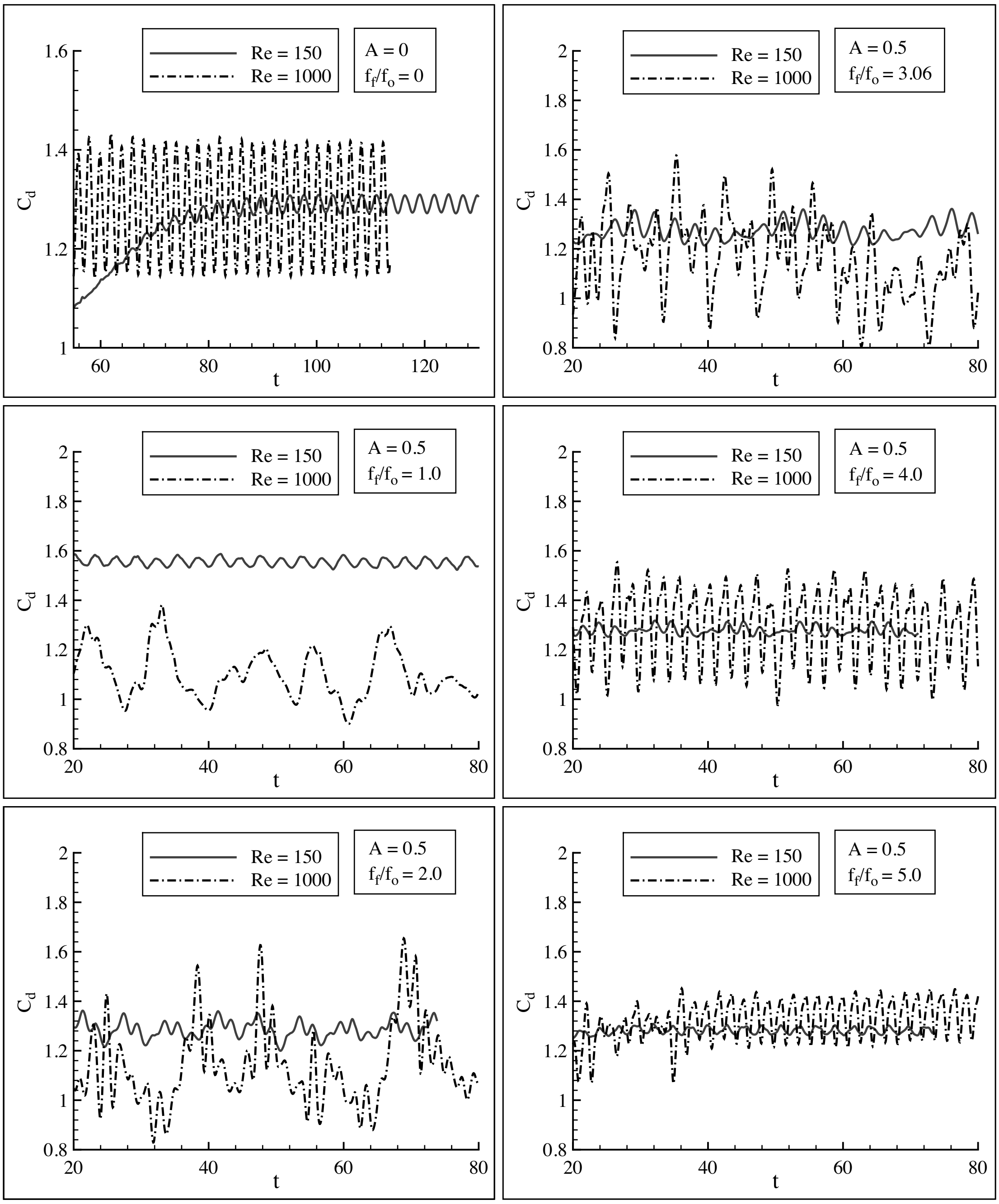

Fig. 7 (a). Comparison of time-variation of drag coefficient for A = 0.5; Re = 150 and 1000 at indicated forcing frequencies. Note that the top left figure corresponds to unforced case.

E_d and K_d were the superharomnics of L_d. However, that case corresponded to drag increase, instead of drag reduction.

Reasons that one can obtain such high drag reduction for $Re = 1000$ at $A = 1$ can also be understood from Fig. 9, where we have compared the vorticity contours for this case with the uncontrolled case, for a small time window after the transients have died down. In the figure, the positive vortices are drawn with solid lines and negative ones by dotted lines. There are two reasons for the drag reduction in the controlled cases: (i) the vortices created for the uncontrolled case remain coherent for longer distances in the wake as compared to the controlled case, a testimony for larger drag associated with stronger disturbances created in the uncontrolled case. Also, the vortices in the controlled case form pairs and/ or triplets those interact and dissipate while convecting downstream and (ii) the transverse width of the wake for the uncontrolled case is higher as compared to the controlled case, that also points to higher

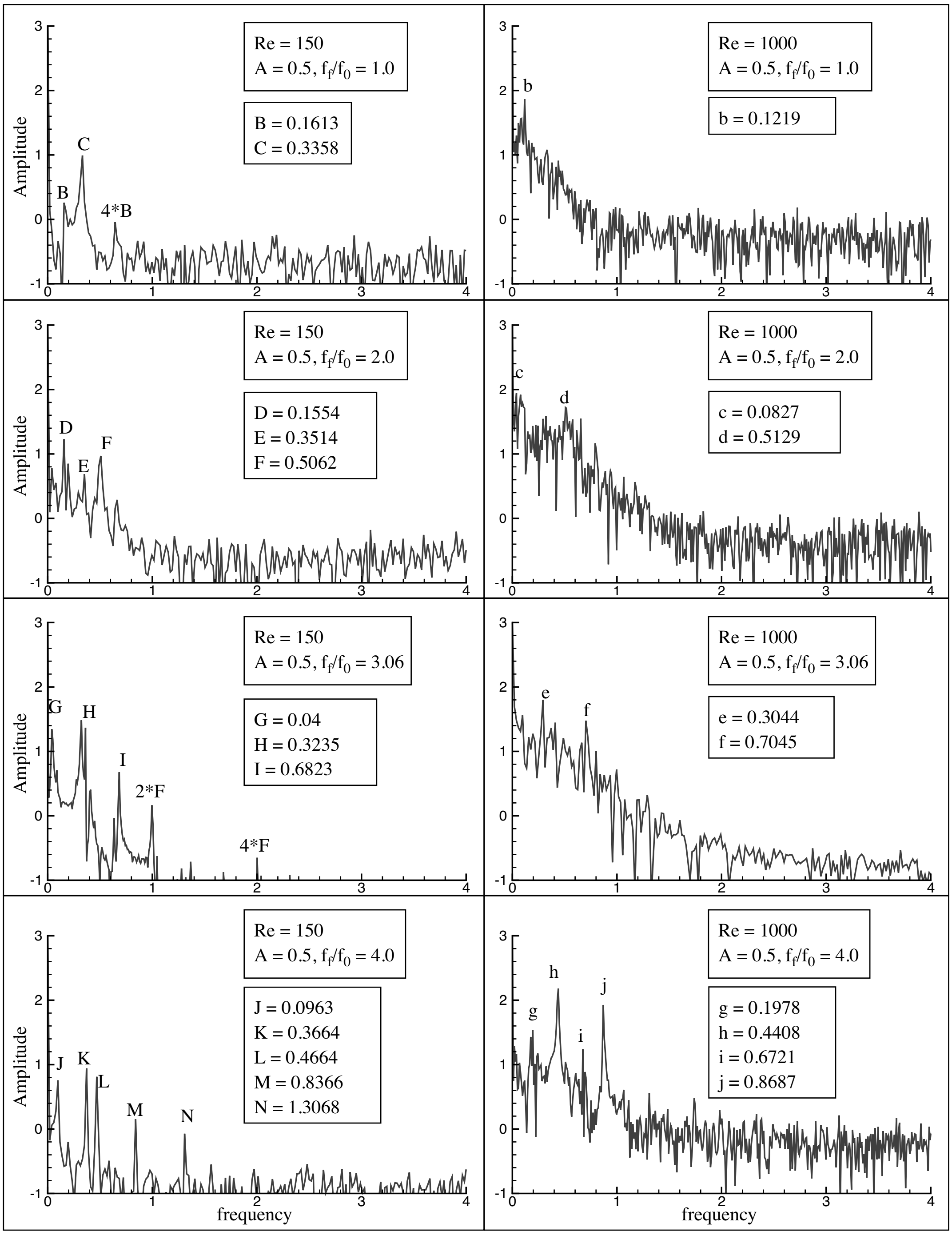

Fig. 7(b). Comparison of Fourier transform of the drag data for the two Reynolds number cases shown in Fig. 7(a) . Here amplitudes are in logarithmic scale. The major frequencies have been identified for different frequency of excitation for a fixed amplitude of rotary oscillation.

drag for the uncontrolled case. For other controlled cases, the drag reduces to a lesser extent, with shed vortices do not cancel pairwise in the far-wake as compared to the case of $A = 1$ shown in Fig. 9.

3.5 Proper Orthogonal Decomposition of Flow Field for Controlled Cases

In many fluid flow problems, as in the present case, coherent structures are present those can be defined with the help of proper orthogonal decomposition (POD), as discussed in Holmes *et al*. [42]. Here the numerical data over the full domain is used for POD by using the method of snapshots due to Sirovich [43].

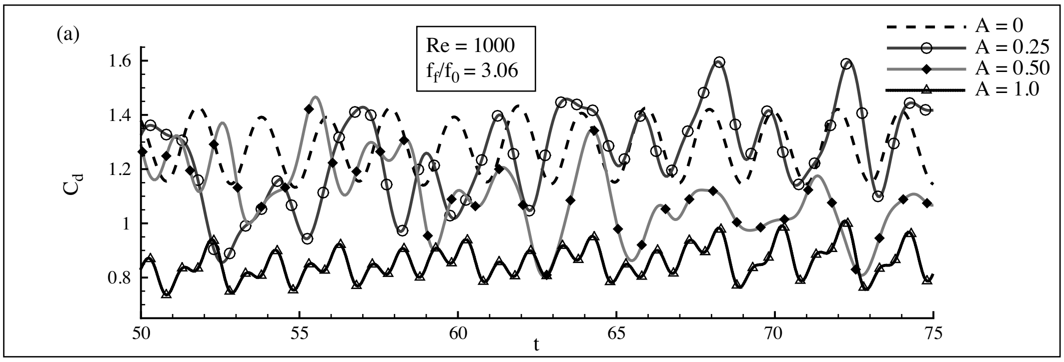

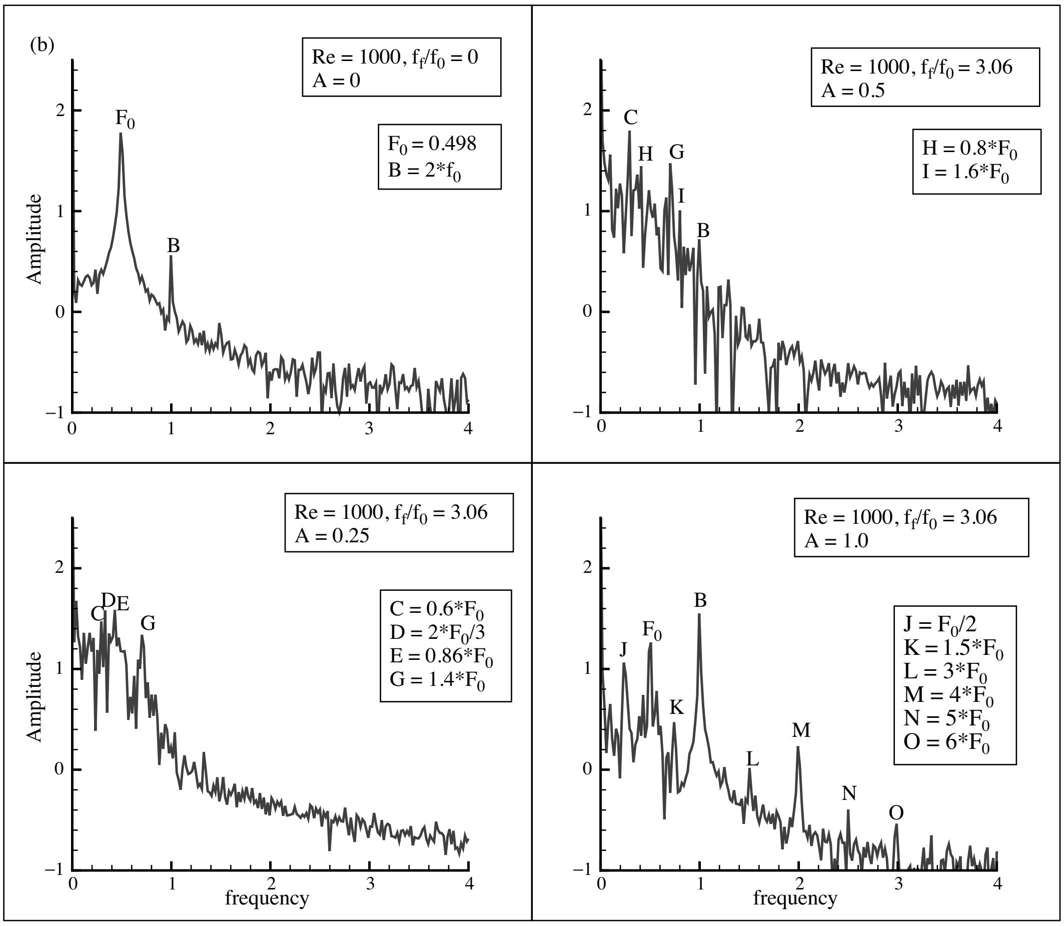

Fig. 8(a). Time variation of the drag coefficient for the case of Re=1000 and $f_f/f_0 = 3.06$ for different amplitudes of rotary oscillation (top) and (b) Fourier transform of the drag data for the indicated parameters. Here the amplitudes are in logarithmic scale. Note the sub- and super- harmonics present for the case of A=1.0, which represents the lowest drag case for this Reynolds number.

In this method, a number of snapshots M, are used for POD analysis that is significantly smaller than the total grid points used for the computation. Data obtained by simulation provide the ensemble of snapshots taken at M instants in time. If one defines the time-varying part of the vorticity field as, $\omega'(x,t) = \sum_{m=1}^{M} a_m(t)\,\phi_{m(x)}$, then ϕ_m are obtained as eigenvectors of the covariance matrix whose elements are defined as $R_{ij} = (1/M)\sum_{m=1}^{M}\omega'(x_i, t_m)\,\omega'(x_i, t_m)$, with $i, j = 1, 2, \ldots, N$ defined over all the points in the domain. The eigenvalues and eigenvectors of $[R_{ij}]$ provide a statistical measure of different dominant modes of the time-varying field. Specifically the eigenvalue gives the probability of

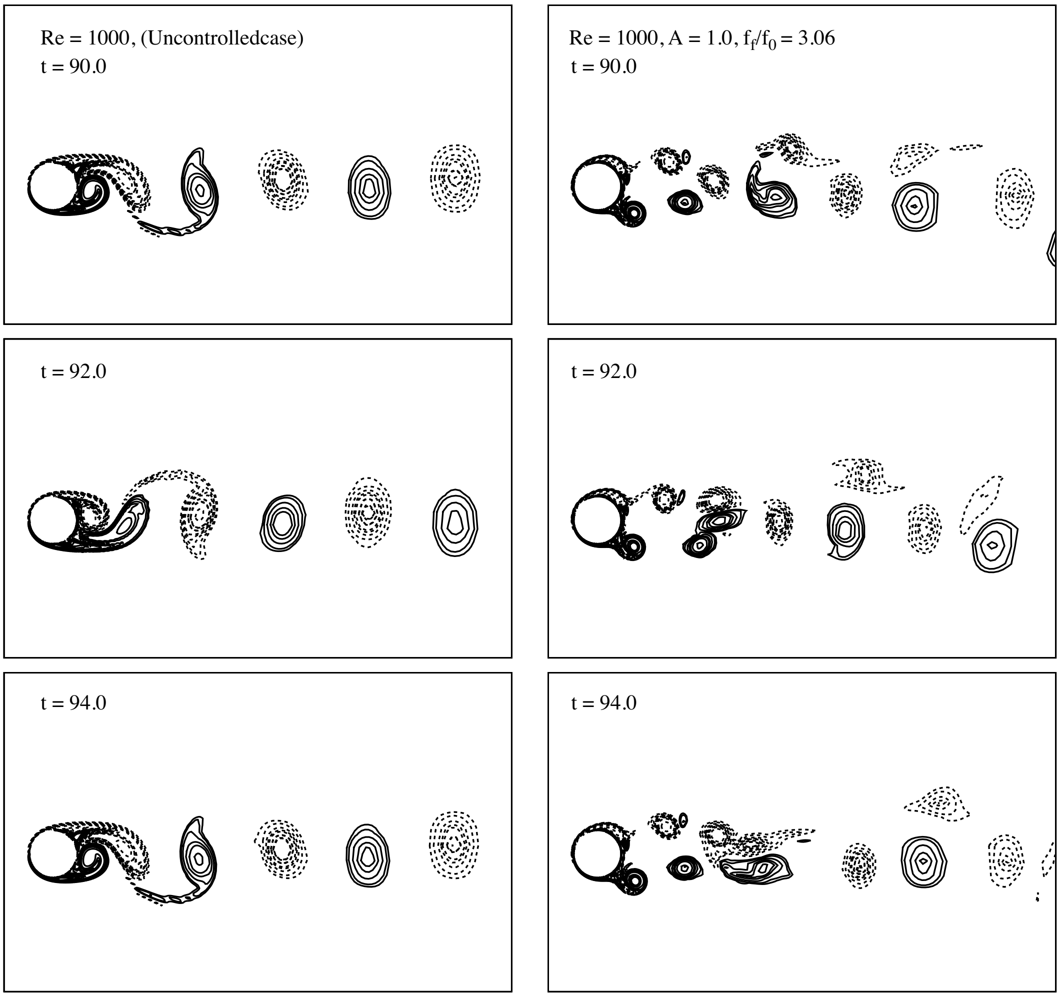

Fig. 9. Comparison of the vorticity contours between the uncontrolled and the controlled case for Re = 1000 case at the indicated times. The controlled case corresponds to the least drag.

occurrence of different modes and their cumulative sum gives the total enstrophy of the system. Such details about the flow control for this geometry can also be seen in Dipankar *et al*. [31].

In Fig. 4 we have noted the completely opposite variations of C_D at same f_f/f_0 for two different Reynolds numbers. For the case of $A = 0.5$ and $f_f/f_0 = 1.0$, C_D attains the highest value for $Re = 150$. In contrast, for $Re = 1000$ at the same f_f/f_0, C_D was seen to be the minimum. This behavior is studied with the help of POD. For the case of $Re = 150$ and $f_f/f_0 = 1$, we have performed POD analysis by using 39 snapshots from $t = 44$ to 82 at equal intervals. For $Re = 1000$, thirtyfive snapshots were used from $t = 150$ to 235 at an interval of $\Delta T = 2.5$. These time ranges preclude capturing any transient effects.

In Fig. 10(a), the cumulative enstrophy contents of different modes are plotted along with the three leading eigenvectors for the case of $Re = 150$. The first two modes account for more than 95% of the total enstrophy. The vortical structures in the first two modes are coherent, those survive over the full computational domain. The third mode is also coherent, but structurally different and that disappear beyond $x = 10d$. While plotting contour plots for the first three eigenvectors, 50 equispaced contour levels are used between –50 and 50. Contour values are identified by an integer that can be obtained from the stated range and number of contour levels. For the case of $Re = 1000$ with the same rotational parameters, the corresponding eigenvalue information and eigenvectors are shown in Fig. 10(b). Here in contrast, the first two modes account for 80% of total enstrophy. The cumulative contributions by successive modes for the higher Reynolds number are comparatively lower. While only first four modes account for more than 99% of total enstrophy for $Re = 150$, one would require 14 modes to describe the same level of enstrophy for $Re = 1000$. For the first three eigenvectors shown in Fig. 10(b), we have

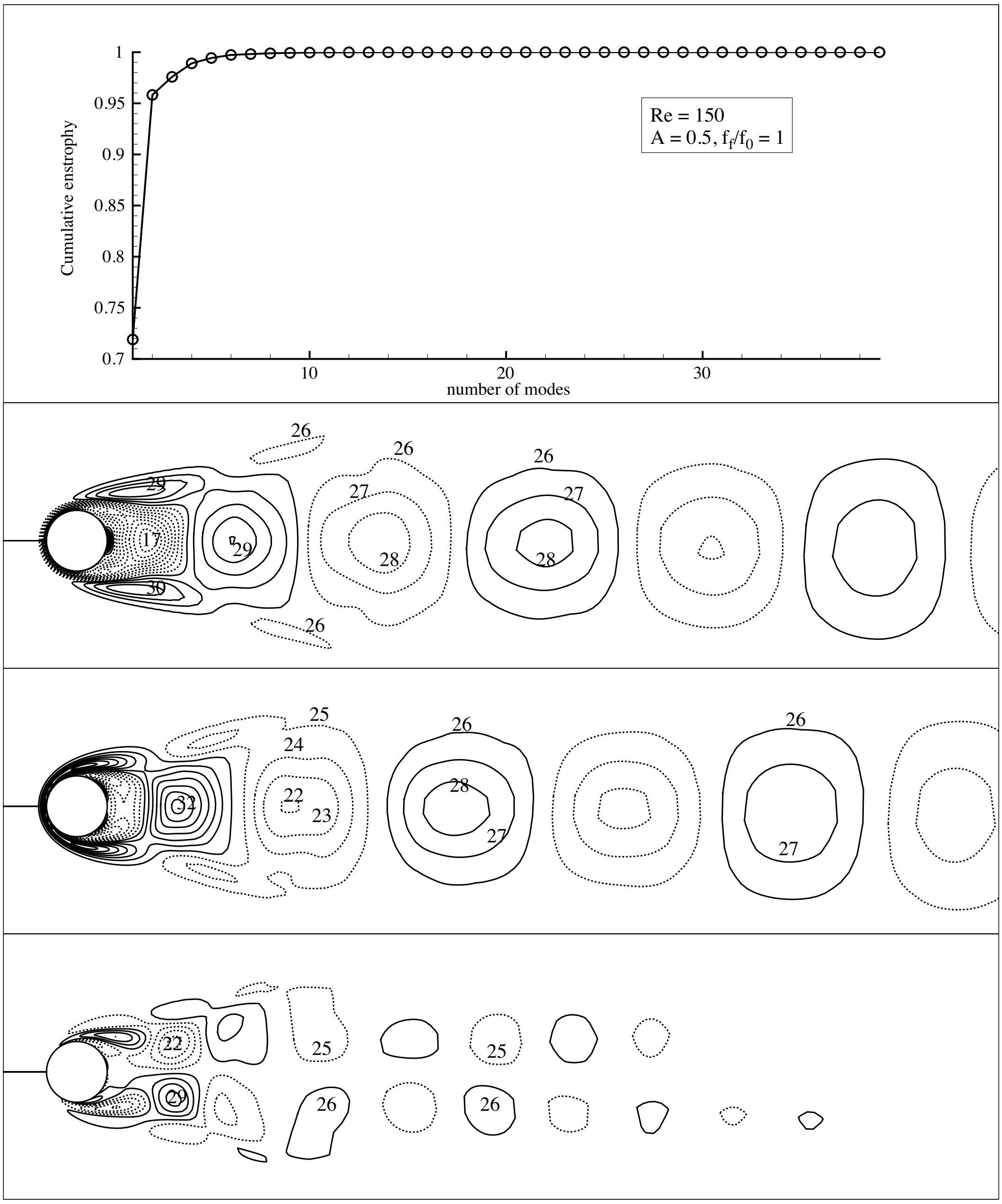

Fig. 10(a). POD analysis for Re = 150; A = 0.5 and f_f / f_0 = 1 case. Top frame indicates cumulative enstrophy distribution among the eigen modes using data from t = 44 to 82. The bottom three frames are the corresponding eigen functions. Note that this controlled case actually results in drag increase compared to the uncontrolled case. Contour levels are as described in the text.

shown 200 contours between –100 to 100. For this case, the eigenvectors are characterized by the absence of large scale coherent vortices in the wake, as compared to the lower Reynolds number case. This shows that the larger coherent structures are responsible for the higher drag at Re = 150, while their breaking up into smaller structures causes the drag to be lower for Re = 1000, as compared to the corresponding uncontrolled case.

In Fig. 6(c), we plotted the variation of drag coefficient for Re = 150 with A for f_f/f_0 = 3.06 and noted two drag minima at A = 0.8 and A = 2. In the following, we identify differences between these drag minima with the help of POD in Fig. 11(a) and 11(b). For A = 0.8, a total of 41 snapshots are taken from t = 70 to 150, at an interval of ΔT = 2. In Fig. 11(a), cumulative enstrophy contents of different modes

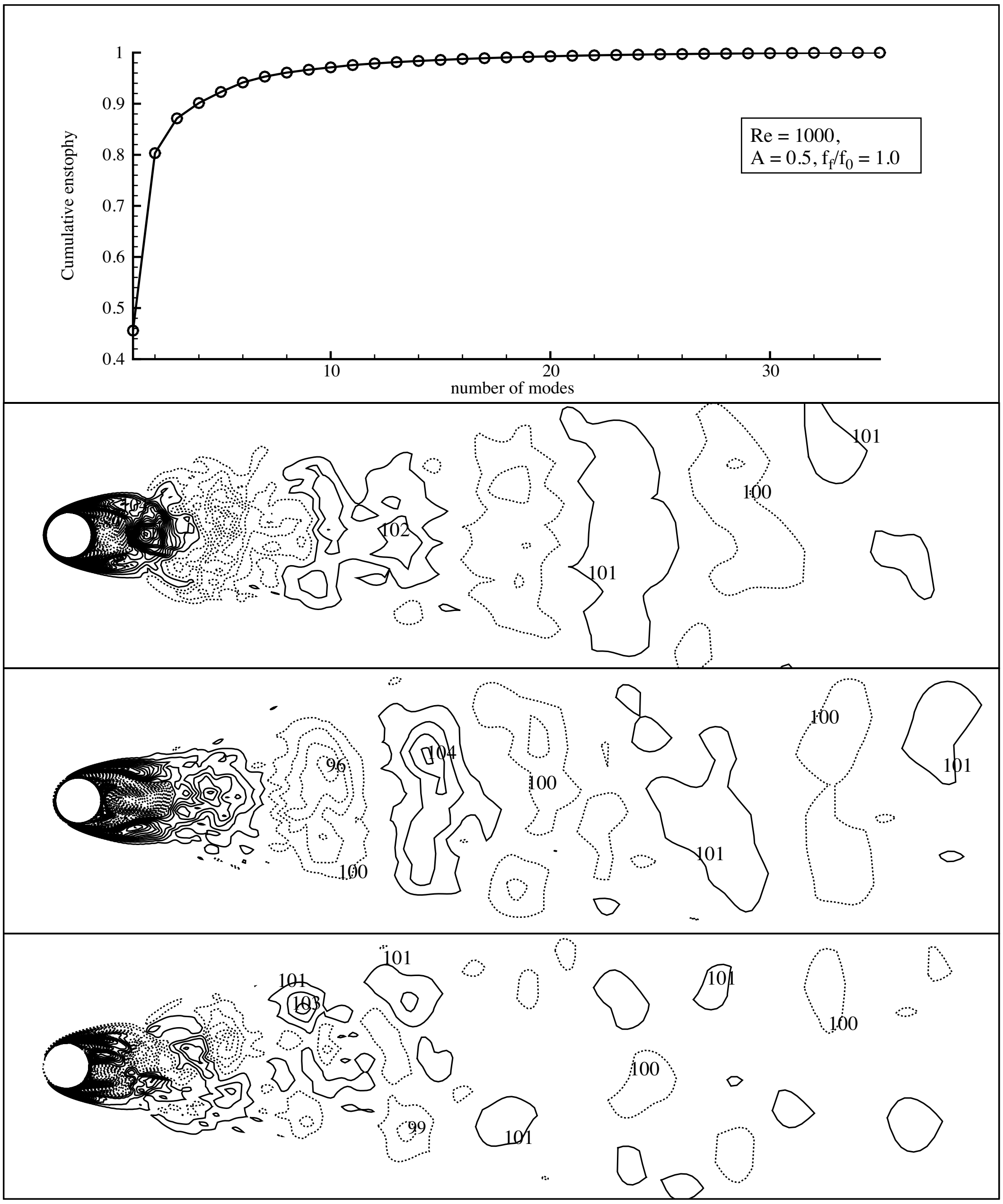

Fig. 10(b). POD analysis for Re = 1000; A = 0.5 and f_f / f_0 = 1 case. Top frame indicates cumulative enstrophy distribution among the eigen modes using data from t = 150 to 235. The bottom three frames are the corresponding eigen functions. Note that this controlled case results in drag reduction. Contour levels are as described in the text.

along with the first three eigenvectors are shown. The first three modes account for 95% of total enstrophy, with the first mode carrying 59% of the enstrophy. In the plotted eigenvectors, 50 contours are plotted in the range of –25 to 25. One also notices that the maximum and minimum of enstrophy levels for this case is half of that was shown in Fig. 10(a), where we noted drag increase. However, the large coherent structures are similar for the first two modes. The third mode here is not as coherent as it was in Fig. 10(a). Thus, one concludes that the wake structure remains same for this case, only the lowering of the disturbances in the wake is responsible for lower drag. For the case of A = 2, there is a qualitative difference of the flow field. as shown in Fig. 11(b). Firstly, we note the enstrophy contents of successive mode reduces significantly. The first mode now accounts for only 30%, as compared to 59% of total enstrophy for the case shown in Fig. 11(a). Also, to account for 95% of enstrophy, one needs only three modes for the case of A = 0.8, the same requires taking 11 modes for the lowest drag

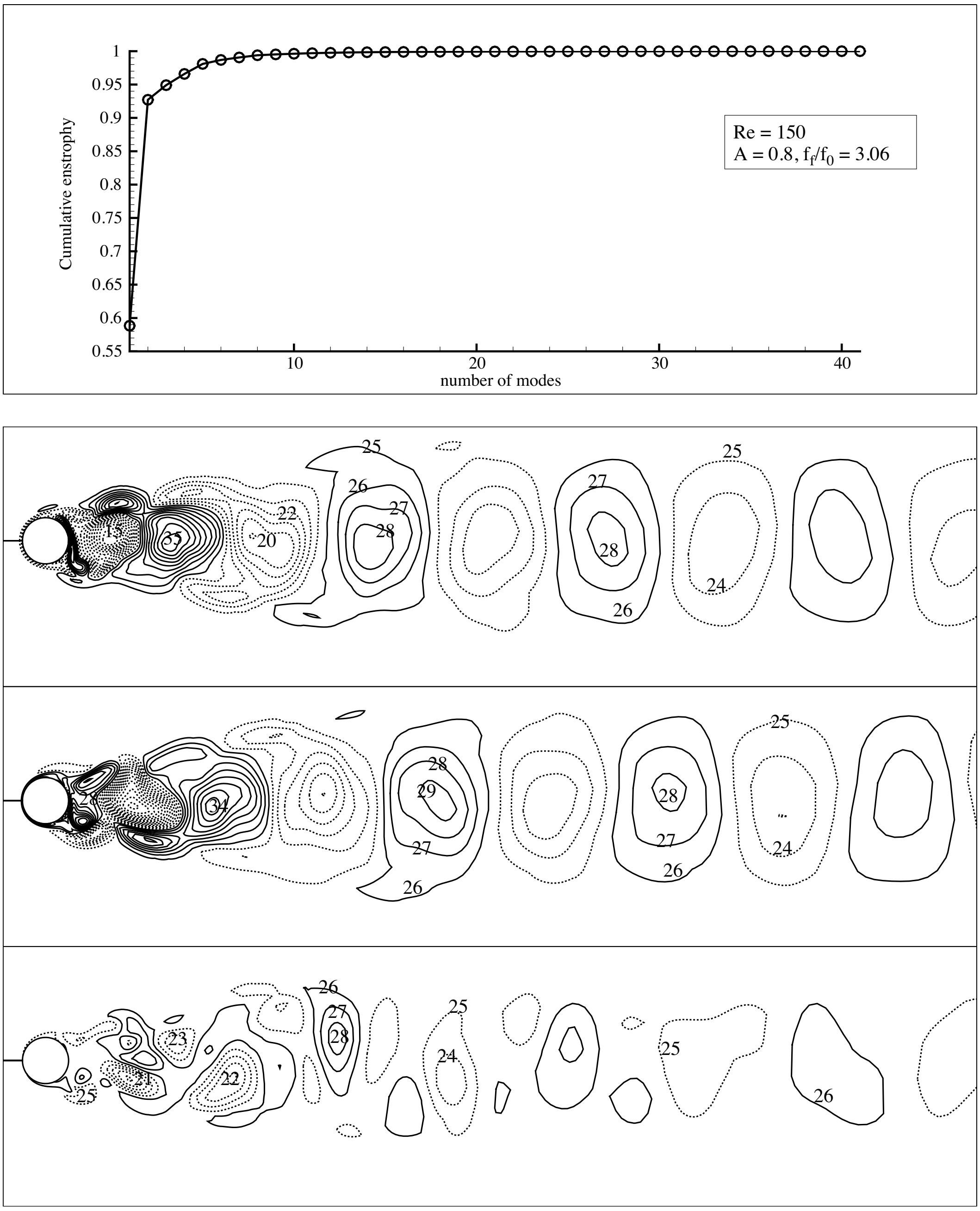

Fig. 11(a). POD analysis for Re = 150; A = 0.8 and f_f / f_0 = 3.06 case. Top frame indicates cumulative enstrophy distribution among the eigen modes using data from t = 70 to 150. The bottom three frames are the corresponding eigen functions. Note that this is a suboptimal drag reduction case. Contour levels are as described in the text.

case of $A = 2$. For the POD analysis in Fig. 11(b), we have taken 32 snapshots between $t = 70$ and 132 at an interval of $\Delta T = 2$. For the displayed seven leading eigenvectors in Fig. 11(b), we have taken 30 contours between –2.5 and 2.5. Here, seven eigenvectors are required to account for 90% of total enstrophy. Also, lower dynamic range reveals lower drag for this case than the cases shown in Fig. 11(a). From the plotted eigenvectors, one can notice the qualitatively different vortical structures for the first two modes. Here the structures are like an arrowhead all the way to the end of the domain. In Fig. 11(a), such weak arrowheads are noted only in the near-wake. These mode shapes are prototypical of cases displaying significant drag reduction for lower Reynolds numbers - as noted in the pair of first and second modes.

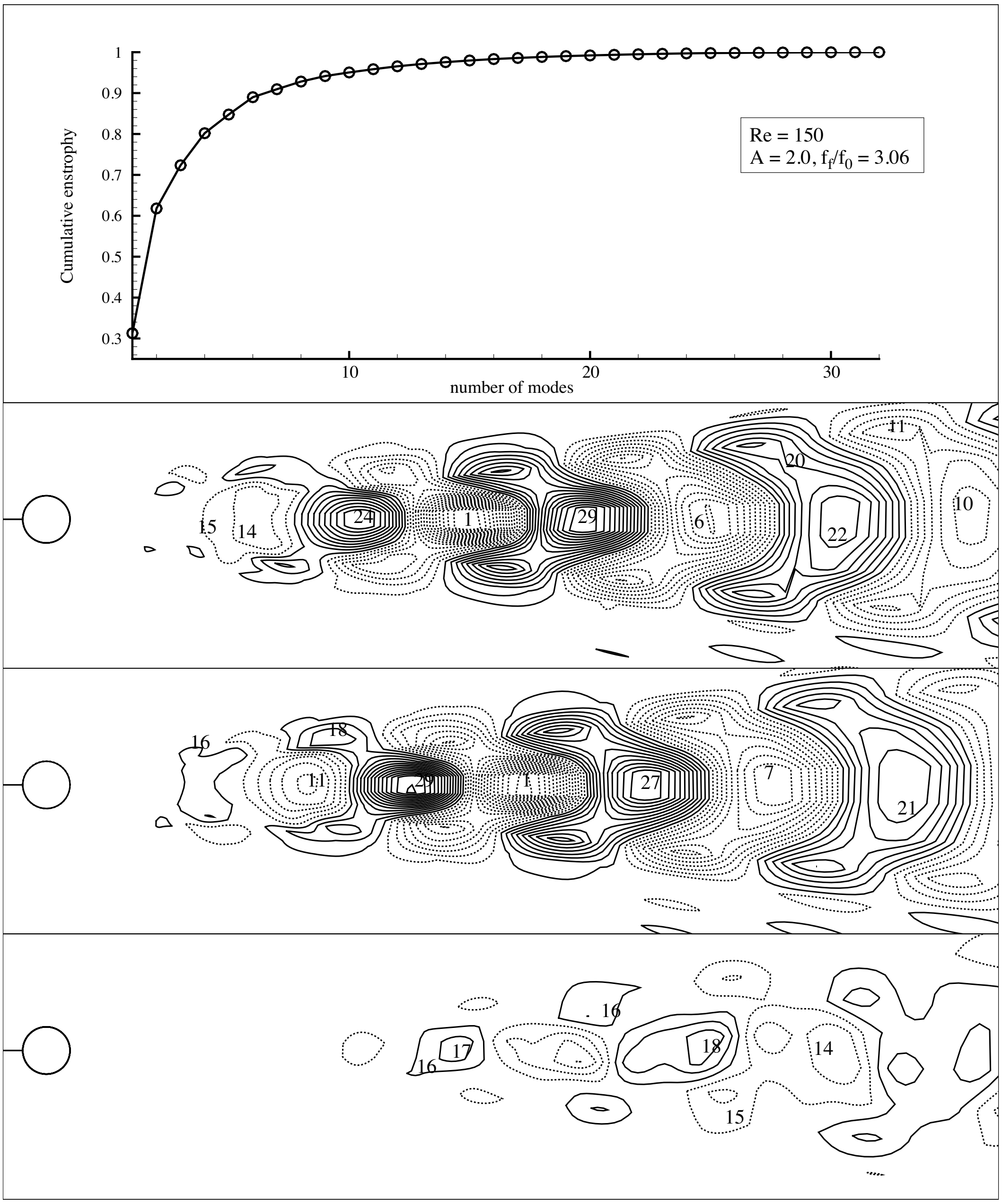

Fig. 11(b). POD analysis for Re = 150; A = 2.0 and f_f / f_0 = 3.06 case. Top frame indicates cumulative enstrophy distribution among the eigen modes using data from t = 70 to 132. The bottom three frames are the corresponding eigen functions. Note that this is an optimal drag reduction case. Contour levels are as described in the text. (Cont.)

These results help us to understand the flow structures when drag reduction is achieved. For the uncontrolled cases or the cases where one instead notices drag increase, the flow is characterized by single coherent persisting vortical structures in the wake. Upon the application of control, the above vortical structures transform in an arrowhead configuration. Appearance and sustenance of such arrowheads in the eigenmodes indicate drag minimum for low Reynolds numbers. The importance of these arrowheads, in realizing large drag reduction at low Reynolds number can be further appreciated by comparing the sub-optimal drag reduction case shown in Fig. 11(a) with the global minimum case shown in Fig. 11(b). In the former figure, the arrowheads just make their appearance, while it is fully formed in Fig. 11(b). However, for higher Reynolds number the vortical structures in the near-wake are fine-grained and do not show arrowhead-like eigenmodes, as shown in Fig. 10(b) for *Re* = 1000.

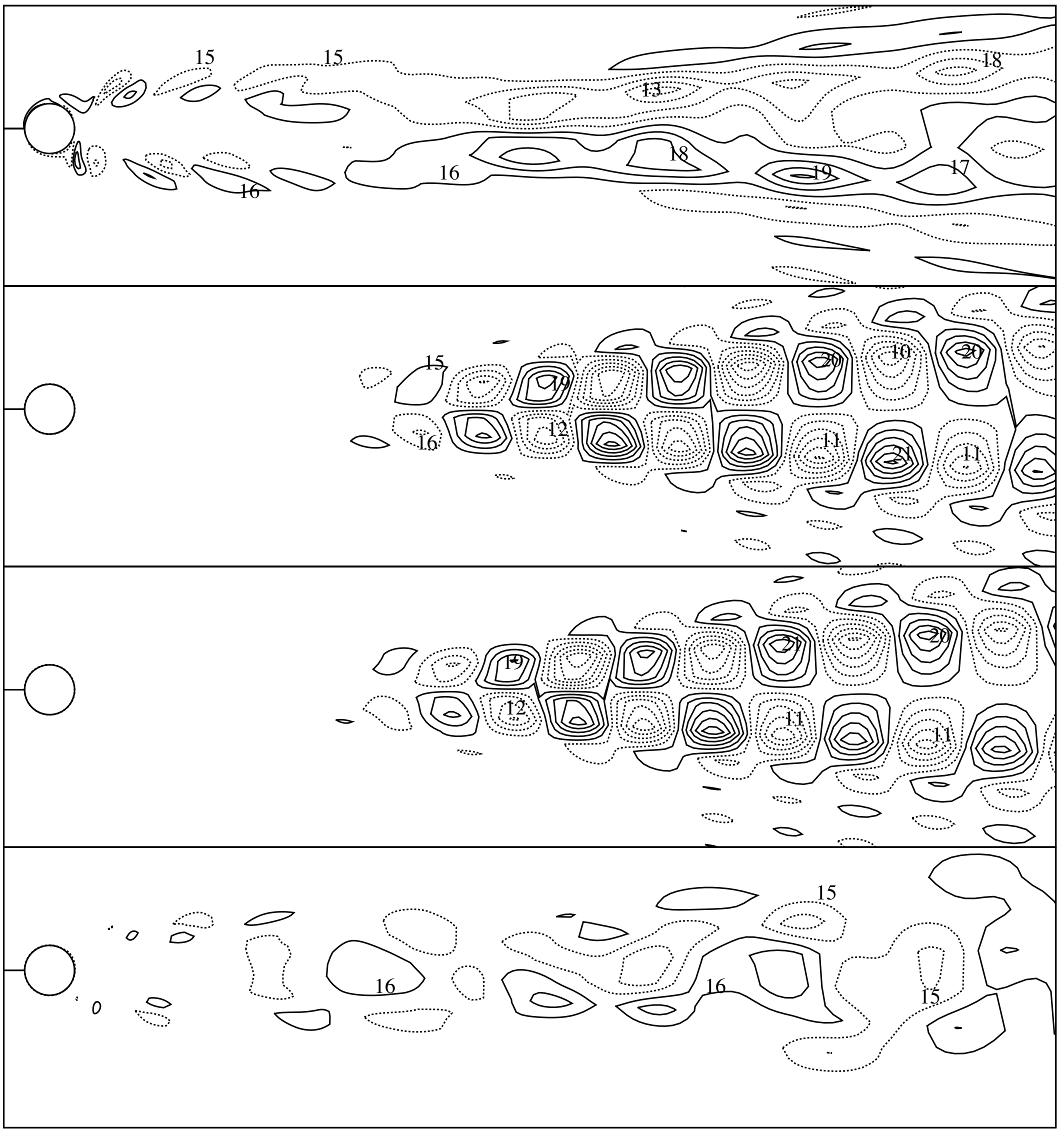

Fig. 11(b). POD analysis for Re = 150; A = 2.0 and f_f/f_0 = 3.06 case. The frames are for fourth to seventh eigen functions- all of which accounts for 90% of total enstrophy. Contour levels are as described in the text.

3.6 Energy Spectrum of Bluff-Body Flows

The energy spectrum of the flow past a stationary circular cylinder is qualitatively different from that representing steady flow past streamlined bodies- due to unsteadiness of the flow for $Re > 45$. For high Reynolds number turbulent flows, injected energy at the large scale cascades down to smaller scales via vortex stretching - a mechanism absent for two-dimensional flows. Thus, small-scale vortices seen in two-dimensional simulation of the flow past a circular cylinder executing rotary oscillation cannot be explained by this stretching mechanism. A specific instability mechanism was shown theoretically and experimentally, in Sengupta *et al*. [27] and Lim *et al*. [28] that created spanwise small-scale vortices in a boundary layer. This mechanism can be present for both two- and three-dimensional flows. Here we show this mechanism also to be present, using the two-dimensional simulation results. For the present problem Shiels & Leonard [26] have also noted the forcing could impose strong two-dimensionality on the near-wake. The essential idea [27] is that any small scale vortex created near the surface is a consequence of the growth of disturbance energy via a dispersion mechanism. The disturbance energy can be expressed as given in the following. If Navier-Stokes equation is expressed in rotational form for incompressible flows, then the quantity $\left(\frac{p}{\rho} + \frac{1}{2}V^2\right)$, is recognized as the mechanical energy *(E)* of the flow and its instantaneous distribution can be described by an equation derived by taking divergence of the Navier-Stokes equation in rotational form to give,

$$\nabla^2 E = \nabla \cdot (VX\omega), \tag{10}$$

If physical quantities are further split into primary and disturbance components by identifying them with subscripts *m* and *d* respectively, then it can be shown that the distribution of disturbance component of mechanical energy is governed by its linearized form of equation (10),

$$\nabla^2 E_d = 2\omega_m \cdot \omega_d + Vm \cdot \nabla^2 V_d + V_d \cdot \nabla^2 V_m \tag{11}$$

Equations (10) and (11) can be used to explain various phenomena observed for bluff-body flows. First and foremost, we can distinguish two-dimensional and three-dimensional flow evolution, by noting the mechanical energy of the flow as a consequence of forcing given by the right hand side of equations (10) and (11). In these equations, the right hand side is stronger in two-dimensional flows, due to the fact that V and ω are always mutually orthogonal. In comparison for three-dimensional flows, component of velocity field that is orthogonal with the vorticity field will contribute to the forcing term on the right hand side of equation (10). Similarly, in equation (11), ω_m and ω_d are parallel to each other for two-dimensional disturbance and primary fields. It will not be so, when either the primary or the disturbance field is three-dimensional. In the same way, V_m and V_d are respectively, parallel to $\nabla^2 V_d$ and $\nabla^2 V_m$ for two-dimensional primary and disturbance field. For vortex dominated flows, this mechanism of energy production was found in Sengupta *et al.* [27] to be responsible for directly creating small-scale vortices, bypassing the more commonly known stretching mechanism for energy cascade. When this bypass mechanism is present for two-dimensional flows, it causes larger production of disturbance energy as compared to that for three-dimensional flows by this bypass mechanism and is relatively weaker. Additional small-scale vortices can be created by the vortex stretching mechanism also. The fact that two-dimensional bluff-body flows display larger loads, wake-width and shorter formation length, indicate that the bypass mechanism is the stronger of the mechanisms for energy cascades discussed above.

We have calculated the right hand side of equation (10) for the two cases of $Re = 150$ and $Re = 1000$ with $A = 0.5$ and $f_f/f_0 = 1.0$ at different time levels to show the effective forcing for the creation of disturbance energy. In Fig. 12, we have compared the right hand side of equation (10) for these two Reynolds number cases. The positive right hand side contours are indicated by solid lines while the negative contours are indicated by dotted lines. As noted in Sengupta *et al.* [27], the positive right hand side indicates location of an energy sink, while negative right hand side indicates locally a source of disturbance energy. For $Re = 150$, one notes formation of triplets or a group of three vortices composed of two sinks and a source of disturbance energy. As time progresses, this group moves together towards the outflow. Such formation of groups can be observed for $Re = 1000$ also, but the size of individual groups are small as compared to the $Re = 150$ case. Also the groups disappear rapidly as they move away from the cylinder. This kind of energy structure results in a lower drag coefficient for $Re = 1000$, as compared to the $Re = 150$ case.

Finally, a brief summary of all the computed cases and the major observations have been provided in Table 1 for the two Reynolds number cases investigated in the present work.

4 CONCLUSION

With very good qualitative and quantitative match between the experimental results in Thiria *et al.* [19] and present numerical simulations, we discuss here two physical mechanisms for drag reduction for flow past a circular cylinder undergoing rotary oscillations. There is a qualitative difference as to how rotary oscillation parameters alter the flow differently for different Reynolds numbers, different amplitudes (*A*) and frequency of rotary oscillation (f_f/f_0). Normalized time-averaged drag coefficient has opposite behavior for $Re = 150$ and $Re = 1000$ for the same forcing amplitude, as shown in Fig. 4. Different A gives rise to different vorticity dynamics, as seen in Fig. 5. This helps us understand the effect of *A* in creating flapping vortices [19] next to the cylinder that controls the dynamics of the flow.

Detailed load distribution for different *A* at a fixed frequency ($f_f/f_0 = 3.06$) are shown in Fig. 6 to identify the optimal *A* for which maximum drag reduction is obtained for $Re = 150$, that confirms with

Fig. 12. The comparison of total mechanical energy source/sink distribution for the two Reynolds number with A and f_f/f_0 held constant. The shown contours represent the right hand side of equation (10). Note the creation of the triplets in the wake that remains intact for the lower Reynolds number case as compared to the higher Reynolds number case.

the experimental results [19]. Additionally, one can also locate different minima for time averaged and fluctuating drag for this case, as shown in Fig. 6(c) and 6(d). Different parameters change the spectrum, as the FFT plots in Fig. 6(a) indicate that for $0 < A < 1.0$, display more frequencies than for the cases with $A > 1.0$.

In Fig. 7, the flow behavior for Re = 150 and Re = 1000 have been compared to understand the effects as a function of Reynolds number for different amplitude of excitation cases. For Re = 1000 it is identified that the drag reduction is maximum for A = 1 (as shown in Fig. 8(a)), whereas for Re = 150 this was seen to occur for A = 2 when the forcing frequency is $f_f/f_0 = 3.06$, as shown in Fig. 6(c). The difference in parameter values for control effectiveness at different Reynolds number is traced to the role of non-linearity becoming more important at relatively higher Reynolds number.

From the vorticity contours in Fig. 9 for Re = 1000, one notices the role of A that modifies the von Karman vortex shedding optimally by comparing it with the uncontrolled case. The vortices in the wake

Table 1 Summary of the various computed cases while studying effect of rotary oscillation on drag reduction

Cases	Re	A	f_f / f_0	Comments
1	150	2.0	0.5;0.75;1.0;1.5;2;3;3.06;4.0	Maximum drag for $f_f / f_0 = 0.75$
2	150	5.0	1.0;2.0;3.0;3.06;4.0	Maximum drag for $f_f / f_0 = 1.0$
3	150	0.5	0.4;0.8;1.0;2.0;3.0;3.06;4.0;5.0	Maximum drag for $f_f / f_0 = 1.0$
4	150	0.2;0.4;0.5;0.6;0.8;0.9; 1.0;1.2;1.5;1.65;1.8;1.9; 2.0;2.5;3.0;4.0;5.0	3.06	Global minimum drag for $A = 2.0$
5	1000	0.5	0.5;1.0;2.0;3.06;3.5;4.0;5.0	Minimum drag for $f_f / f_0 = 1.0$
6	1000	0.25;0.5;1.0	3.06	Minimum drag for $A = 1.0$

remain coherent and sustained for the uncontrolled case, whereas for the controlled case, the vortices form pairs and destroy them before they reach the far-wake.

The vorticity dynamics as affected by forcing parameters can also be understood by POD analysis. This helps one to understand in a statistical sense, the number of eigenmodes of the flow and cumulative enstrophy carried by them. Fig. 10 and 11 show that to achieve drag reduction, single, long lasting, coherent structures for the uncontrolled case should be removed by a proper choice of control parameters for $Re = 150$. Also, the enstrophy carried by the first few modes is less for the optimal case, as compared to that for the uncontrolled and high drag cases. In Fig. 11(a) and 11(b), an optimal controlled case is compared with another sub-optimal controlled case. Typical vortical structures those lead to maximum drag reduction are identified as producing arrowhead-like eigenfunctions.

Finally, the energy spectrum of two-dimensional bluff-body flow is investigated with the help of energy based receptivity analysis [27]. This helps one to identify disturbance energy sources and sinks in the near wake, as shown in Fig. 12 for the cases of $Re = 150$ and $Re = 1000$ for $A = 0.5$ and $f_f/f_0 = 1$. From Fig. 4, we have seen that $Re = 150$ the drag actually increased, while for $Re = 1000$ there is large sub-optimal drag reduction. In both the cases shown in Fig. 12, triplets of disturbance energy sinks and a source are identified those remain coherent in the lower Reynolds number case, while for the higher Reynolds numbers such structures are smaller and dissipative.

REFERENCES

[1] Bearman, P.W., 1984. Vortex shedding from oscillating bluff bodies. *Annual Review of Fluid Mechanics* 16, 195–222

[2] Berger, E., Willie, R., 1972. Periodic flow phenomenon. *Annual Review of Fluid Mechanics* 4, 313–340.

[3] Griffin, O.M., Hall M.S., 1991. Vortex shedding lock on and flow control in bluff body wakes. *Journal of Fluids Engineering* 113, 526–537.

[4] Sumer, B.M., Fredsϕe, J., 1997. *Hydrodynamics Around Cylindrical Structures*. World Scientific, Singapore.

[5] Williamson, C.H.K., Govardhan, R., 2004. Vortex-induced vibrations. *Annual Review of Fluid Mechanics* 36, 413–455.

[6] Badr, H.M., Coutanceau, M., Dennis, S.C.R., Menard, C., 1990. Unsteady flow past a rotating circular cylinder at Reynolds numbers 10^3 and 10^4. *Journal of Fluid Mechanics* 220, 459–484.

[7] Chang, C.C., Chern, R.L., 1991. Vortex shedding from an impulsively started rotating and translating circular cylinder. *Journal of Fluid Mechanics* 233, 265–298.

[8] Chen, Y.M., Ou, Y.R., Pearlstein, A.J., 1993. Development of the wake behind circular cylinder impulsively started into rotary and rectilinear motion. *Journal of Fluid Mechanics* 253, 449–484.

[9] Sengupta, T.K., Kasliwal, A., De, S., Nair, M., 2003. Temporal flow instability for Magnus-Robins effect at high rotation rate. *Journal of Fluids and Structures* 17, 941–953.

[10] Diaz, F., Gavalda, J., Kawall, J.G., Keffer, J.F., Giralt, F., 1983. Vortex shedding from a spinning cylinder. *Physics of Fluids* 26(12), 3454–3460.

[11] Sengupta, T.K., Deb, K., Talla, S.B., 2007. Control of flow using genetic algorithm for a circular cylinder executing rotary oscillation. *Computers and Fluids* 36, 578–600.

[12] Sengupta, T.K., Kumar, G., 2006. Bluff-body flow control by aerodynamic tripping. In : *ASME PVT 2006/ ICPVT-11 Conference on Flow-Induced Vibration*, Vancouver, Canada.

[13] Dennis, S.C.R., Nguyen, P., Kocabiyik, S., 2000. The flow induced by a rotationally oscillating and translating circular cylinder. *Journal of Fluid Mechanics* 407, 123–144.

[14] Taneda, S., 1978. Visual observations of the flow past a circular cylinder performing a rotary oscillation. *Journal of the Physical Society of Japan* 45, 1038–1043.

[15] Okajima, A., Takata, H., Asanuma, T., 1975. *Viscous flow around a rotationally oscillating cylinder*. Institute of Space and Aeronautical Science (University of Tokyo) Japan, 532, 311–318.

[16] Wu, J.M., Mo, J.D., Vakili, A.D., 1989. On the wake of a cylinder with rotational oscillations. In *2nd AIAA Shear Flow Conference*, Tempe, Az, pp. Paper No. AIAA-1989–1024.

[17] Tokumaru, P.T., Dimotakis, P.E., 1991. Rotary oscillation control of a cylinder wake. Journal of Fluid Mechanics 224, 77–90.

[18] Filler, J.R., Marston, P.L., Mih, W.C., 1991. Response of the shear layers separating from a circular cylinder to small-amplitude rotational oscillations. *Journal of Fluid Mechanics* 231, 481–499.

[19] Thiria, B., Goujon-Durand, S., Wesfreid, J.E., 2006. The wake of a cylinder performing rotary oscillations. *Journal of Fluid Mechanics* 560, 123–147.

[20] Lu, X.Y., Sato, J., 1996. A numerical study of flow past a rotationally oscillating circular cylinder. *Journal of Fluids and Structures* 10(8), 829–849.

[21] Baek, S.J., Sung, H.J., 1998. Numerical simulations of the flow behind a rotary oscillating circular cylinder. *Physics of Fluids* 10, 869–876.

[22] Cheng, M., Chew, Y.T., Luo, S.C., 2001. Numerical investigation of a rotationally oscillating cylinder in mean flow. *Journal of Fluids and Structures* 15, 981–1007.

[23] Choi, S., Choi, H., Kang, S., 2002. Characteristics of flow over a rotationally oscillating cylinder at low Reynolds number. *Physics of Fluids* 14(8), 2767–2777.

[24] Protas, B., Styczek, A., 2002. Optimal rotary control of the cylinder wake in the laminar regime. *Physics of Fluids* 14(7), 2073–2087.

[25] He, J.W., Glowinsky, R., Metcalfe, R., Nordlander, A., Periaux, J., 2000. Active control and drag optimization for flow past a circular cylinder. *Journal of Computational Physics* 163, 83–117.

[26] Shiels, D., Leonard, A., 2001. Investigation of a drag reduction on a circular cylinder in rotary oscillation. *Journal of Fluid Mechanics* 431, 297–322.

[27] Sengupta, T.K., De, S., Sarkar, S., 2003. Vortex-induced instability of incompressible wall-bounded shear layer. *Journal of Fluid Mechanics* 493, 277–286.

[28] Lim, T.T., Sengupta, T.K., Chattopadhayay, M., 2004. A visual study of vortex-induced subcritical instability on a flat plate laminar boundary layer. *Experiments in Fluids* 37, 47–55.

[29] Protas, B., Wesfreid, J.E., 2002. Drag force in the open-loop control of the cylinder wake in the laminar regime. *Physics of Fluids* 14(2), 810–826.

[30] Sengupta, T.K., Sircar, S.K., Dipankar, A., 2006. High accuracy schemes for DNS and acoustics. *Journal of Scientific Computing* 26(2), 151–193.

[31] Dipankar, A., Sengupta, T.K., Talla, S.B., 2007. Suppression of vortex shedding behind a circular cylinder by another control cylinder at low Reynolds numbers. *Journal of Fluid Mechanics* 573, 171–190.

[32] Williamson, C.H.K., 1988. The existence of two stages in the transition to three dimensionality of a cylinder wake. *Physics of Fluids* 31, 3165–3168.

[33] Khalak, A., Williamson, C.H.K., 1996. Dynamics of hydrostatic cylinder with very low mass damping. *Journal of Fluids and Structures* 10, 455–472.

[34] Poncet, P., 2002. Vanishing of mode B in the wake behind a rotationally oscillating circular cylinder. *Physics of Fluids* 14(6), 2021–2023.

[35] Poncet, P., 2004. Topological aspects of three-dimensional wakes behind rotary oscillating cylinders. *Journal of Fluid Mechanics* 517, 27–53.

[36] Esposito, P.G., Verzicco, R., Orlandi, P., 1993. Boundary condition influence on the flow around a circular cylinder. In the *proceedings of IUTAM Symposium on Bluff-Body Wakes, Dynamics and Instabilities*, Springer-Verlag, Berlin, Germany, 47–50.

[37] Orlanski, I., 1976. A simple boundary condition for unbounded hyperbolic flows. *Journal of Computational Physics* 21, 251–269.

[38] Van der Vorst, H.A., 1992. BI-CGSTAB: A fast and smoothly converging variant of Bi-CG for the solution of non-symmetric linear systems. *SIAM Journal of Scientific and Statistical Computing* 13(2), 631–644.

[39] Saad, Y., 2003. *Iterative Methods for Sparse Linear Systems*. SIAM, USA.

[40] Sengupta, T.K., Ganeriwal, G., De, S., 2003. Analysis of central and upwind compact schemes. *Journal of Computational Physics* 192(2), 677–694.

[41] Henderson, R.D., 1997. Nonlinear dynamics and pattern formation in turbulent wake transition. *Journal of Fluid Mechanics* 352, 65–112.

[42] Holmes, P., Lumley, J.L., Berkooz, G., 1996. *Turbulence, Coherent Structures, Dynamical Systems and Symmetry*. Cambridge Univ. Press, UK.

[43] Sirovich, L., 1987. Turbulence and dynamics of coherent structures, Part I- III. *Quarterly of Applied Mathematics* 45(3), 561–590.